Investigation and quantification of cell-type diversity in three-dimensional primary cortical tissue model of Alzheimer's Disease

By Abigail Drexler
B.Sc. University of California, Los Angeles, 2019

Thesis

Submitted in partial fulfillment of the requirements for the Degree of Master of Science in Biomedical Engineering at Brown University

PROVIDENCE, RHODE ISLAND
MAY 2024

AUTHORIZATION TO LEND AND REPRODUCE THE THESIS

As the sole author of this thesis, I authorize Brown University to lend it to other institutions or individuals for the purpose of scholarly research.

Date 4/24/24

Abigail Drexler, Author

I further authorize Brown University to reproduce this thesis by photocopying or other means, in total or in part, at the request of other institutions or individuals for the purpose of scholarly research.

Date 4/24/24

Abigail Drexler, Author

This thesis by Abigail R. Drexler is accepted in its present form by the Center of Biomedical Engineering as satisfying the thesis requirement for the degree of Master of Science.

Date 4/24/2024

Dr. David Borton, Associate Professor of Engineering, Associate Professor of Neurosurgery, Associate Professor of Brain Science, Advisor

Recommended to the Graduate Council

Date 4/24/24

Dr. Sonia Mayoral, Robert J. and Nancy D. Carney Assistant Professor of Neuroscience

Date 4/24/2024

Dr. Yu-Wen Alvin Huang, GLF Translational Assistant Professor of Molecular Biology, Cell Biology and Biochemistry

Date 4/24/2024

Dr. Jeffrey Morgan, Professor of Pathology and Laboratory Medicine, Donna Weiss '89 and Jason Weiss Director of the Center for Alternatives to Animals in Testing, Professor of Engineering

Approved by the Graduate Council

Date 4/24/2024

Dr. Mariss Gray, Biomedical Engineering Master's Program Director

TABLE OF CONTENTS

Abstract

Alzheimer's disease (AD) is the most common form of dementia, estimated to affect over 6 million individuals in the United States in 2024[1,2]. Despite its prevalence, there is still no substantial treatment or cure for this terminal disease. As a result, significant resources have been invested in expanding AD research. Recent advances in AD research have expanded the use of *in vitro* tools with the use of human stem cells and 3D models, as well as transgenic animals modified to carry known genetic mutations and risk genes associated with AD. The central aim of this thesis work was to characterize the use of the AD transgenic rat in a 3D primary cortical cell culture model.

Using a previously developed 3D primary cortical culture model[47], both wild-type (WT) and TgF344-AD transgene positive 'microtissues' were created and cultured over four extended periods (DIV 2, 7, 28, 60) and then labeled with an immunofluorescent tag for confocal microscope imaging. The images were quantitatively evaluated using cell counts, mean fluorescence intensity, and 2D Sholl analysis. Throughout the culture, the supernatants of TgF344-AD 'microtissues' were collected and examined for amyloid-beta-42 via ELISA and later evaluated using immunofluorescence. We observed significant changes in neural progenitor cell counts and significant changes in the mean fluorescence intensity of GFAP-positive astrocytes across the duration of the culture in wild-type microtissues. Additionally, significant changes in microglia morphology, marked by longer and more ramified extensions, were observed at day *in* vitro (DIV) 28 compared to DIV 2. Significant changes in secreted Amyloid Beta (42) were detected by ELISA between WT and TgF344-AD microtissues, as well as significant increases between DIV 6 and DIV 28 in TgF344-AD tissues. In conclusion, this 3D culture system exhibits a diverse and dynamic molecular and cellular environment, capable of being cultured for up to 60 days without an additional scaffold or serums, and applicable for the study of the intricate multicellular mechanisms associated with diseases like AD, with integration of the TgF344-AD rat model.

Background

Alzheimer's Disease

Alzheimer's disease (AD) is the seventh leading cause of death in the United States, with an estimated 6 million adults over the age of 65 suffering from the condition[1-4]. By 2050, the incidence of AD has been predicted to reach 12.7 million[2]. The primary risk associated with developing AD is aging, with the frequency of diagnosis doubling every five years after sixty[2,4-6,]. While AD may be the most common form of dementia, it is also the only disease within the top ten U.S. mortality list without an effective treatment[1-5].

Among the primary clinical presentations of AD, the most notable are memory loss and cognitive impairment, which correspond with the numerous pathologies[1-6]. Alzheimer's is classified as a neurodegenerative disease (NDD), meaning it presents with all of the hallmarks of NDDs: progressive neuron loss and dysfunction, abnormal protein aggregates, and circuit selectivity[7]. The primary circuitry affected in AD is associated with memory and cognition, while the proteins associated with aggregates in AD are amyloid-beta and tau[2,3,6-11]. In AD, neurons and glia secrete large amounts of the Aβ-42 oligomer, resulting in extracellular amyloid-beta plaques rich with the Aβ-42, which coincides with the accumulation of intracellular tau tangles (neurofibrillary tangles)[5, 8-13]. These primary pathogenic hallmarks are associated with neurotoxicity, neuronal dysfunction, and degradation as well as neuroinflammation, linked to glial cell dysregulation, which culminates and ultimately may lead to the clinical presentation of memory and cognitive impairment[3,5,7,9-17].

The understanding of Alzheimer's disease pathogenesis has transformed over the years. The amyloid hypothesis first appeared after the initial discovery of amyloid plaques and tau tangles[18,20]. This hypothesis states that amyloid-beta accumulation is the primary cause of AD, initiating all other associated pathologies[18,20]. However, new evidence has challenged this hypothesis in recent years, expanding the scope of AD research to different cell types, environmental conditions, and interactions[3,19].

Despite many of the molecular dynamics involved in the progression of the disease being unknown, there are recognized genetic variants that increase the risk of developing AD: apolipoprotein E (APOε4), amyloid precursor protein (APP), and presenilin 1 and 2 (PSEN1/2)[21-26]. The penetrance of these variants impacts the progression of the disease and subsequent symptoms onset. APOε4 mutations have a lower penetrance and are associated with sporadic, late-onset AD, while APP and PSEN1/2 variants are considered highly penetrant, familial AD mutations as they are associated with autosomal dominant inheritance, resulting in early-onset AD[2,12,13 23-24]. These known mutations associated with AD have driven recent research through inducing the mutations in induced pluripotent stem cells (iPSCs) or generating transgenic animals[6,16,21,25-29].

Several of these risk factors are highly expressed by glial cells and are known to impact glial cell states, emphasizing the need to understand better the connection between glia and neurons that leads to the characteristic neuron dysfunction and degeneration observed in an AD neural environment [3,14,15,21-25,72]. In healthy neural environments, delicate and specific glial-neuron interactions and signals maintain the homeostatic environment and processes, including amyloid-beta clearance[3,14,15,21-25,72]. However, in the AD brain, there are distinct shifts toward more reactive cell states characterized by changes in morphology, function, and gene expression patterns that lead to a disruption in neuronal support and ultimately may cause neuron loss and dysfunction[21-25,72]. In the current landscape of AD research, there are severe limitations to studying these multicellular mechanisms in patients due to the fact that the majority of data collection is primarily based on MRI and PET scans, which lack the single-cell resolution needed to study these intricate glial-neuron interactions. Ultimately, there is a need for robust and reliable *in vitro* models to study the cellular and molecular mechanisms of glial-neuron interactions in AD pathogenesis.

Current In Vitro Modeling

Alzheimer's has the distinction of being one of the most widely studied and researched diseases without a robust treatment or cure. A significant reason for this is the inherent difficulty

in recapitulating the physiological conditions of neurological diseases and their clinical pathology, which impedes the understanding of disease progression well enough to develop potential therapeutics[28-31]. Currently, a wide array of *in vitro* models aim to tackle these challenges and improve the understanding of Alzheimer's Disease at the molecular level[25,30,31,33,36]. *In vitro* models allow the reproducible study of molecular mechanisms in a controlled environment with an increased throughput compared to *in vivo* models[28,30,44]. These *in vitro* studies consist of both 2D and 3D models and an array of cell sources, ranging from primary cells collected from animal models to human stem cells and primary human cells collected from neural tissue during surgical biopsy and then subsequently cultured *in vitro* for short periods of time. The use of iPSCs has significantly enhanced research efforts as human cells can be used to study human diseases and can be genetically edited to carry the known genetic mutations associated with AD[6,16,27,31-36]. They have been used in both 2D monolayer and 3D models, such as organoids. However, these organoid models are limited due to an inherent lack of neural cell-type diversity and maturity[28,30,36,39,51]. Additionally, many 3D cell culture models require the use of an exogenous scaffold due to the lack of an endogenous extracellular matrix (ECM)[28,30,36,39,51]. This is a critical component of 3D culture models as the ECM plays an essential role in cell signaling and cytoarchitecture, providing both structural and functional support to the surrounding cells[28,30,36,39,51]. 3D post-mortem tissue analysis is also frequently used; however, while this tissue maintains the endogenous cell-type diversity, including ECM, it only provides a snapshot in time of the multicellular interactions from the time of collection. While the culture of primary human neural cells *in vitro* may allow for the evaluation of disease phenotypes in a patient-specific manner, they are difficult to maintain once removed from the brain environment. This transfer of primary human cells from the *in vivo* to the *in vitro* environment poses a significant challenge when studying human microglia, which are among the most sensitive cell types to environmental changes[28,32]. However, these primary cell culture models do allow for the inclusion of a diverse population of endogenous cell types, which facilitates the study of multicellular dynamics in a

controlled system[28,30,40,44]. Primary culture models remain relevant in AD research as they can provide valuable insight into complex cell-to-cell and cell-to-ECM behaviors as they maintain the endogenous, multicellular environment[28,30,44,51].

For this thesis work, we used a scaffold-free 3D rodent-derived primary cortical culture model. Recent studies show that 3D cell culture models better recapitulate an *in vivo*-like environment compared to 2D culture[28,30,33-39,41-50]. While 2D culture models may be ideal for visualizing elements of cellular dynamics like axon and dendritic growth or synapse formation, their physiological relevance is limited by the nature of a monolayer culture[28,30,41-46]. 2D cultures lack the cell-to-cell and cell-to-ECM interactions that allow for the complex cytoarchitecture and metabolic activity characteristic of *in vivo* tissue[28,30,39-45,47-51]. In addition, 2D cultures often require a scaffold to promote cell growth, proliferation, and migration, as they cannot adequately produce and interact with ECM[28,30,40-45,47-51]. Our primary 3D culture model harnesses the cells' innate self-assembly behavior[30,40]. Due to the nature of this primary culture, no additional scaffold is required as the endogenous ECM remains in the culture, facilitating cell growth and neuronal network organization[28,30,40,44,48]. This 3D ‘microtissue’ model is uniquely suited for long-term live imaging due to the 350 ųm offset from the bottom of the plate and the agarose mold that serves as a physical constraint for the microtissue[30,48]. The agarose anchors the tissue to a fixed position and prevents further contraction into a spheroid that would otherwise float within the well. We aimed to create a physiologically relevant 3D model that maintains the operational benefits of *in vitro* tools to study cell-type specific interactions and mechanisms in AD pathogenesis.

While our 3D primary cortical culture model has been used to study neuroinflammation and biomaterial compatibility with implantable devices, an extensive characterization over an extended culture period has yet to be completed[30,48]. Although it appears to be physiologically relevant from the endogenous-ECM-promoted self-assembly and neuroinflammatory response, additional investigation is still required to test the validity of this claim. In addition, we seek to investigate its potential application as a disease model, specifically for Alzheimer’s Disease.

TgF344-AD

Most of the current transgenic animals used in AD research are mice[52-59]. However, even though many of these transgenic AD mouse models experience an overproduction of amyloid-beta, they are simultaneously unable to demonstrate the characteristic neuronal loss and tauopathy[26,52-59]. These transgenic models require additional familial AD mutations to induce the other pathological hallmarks of AD[54,55,57-59]. While the use of mice may be more ubiquitous in AD transgenics, another rationale for their lack of presentation of the physiologically relevant pathologies of AD is the varying relation to humans. Rats are 4-5 million years closer to humans in evolutionary history than mice are, which may impact their physiological relevance to humans as research models[26,60].

The novel rat model, TgF344-AD, developed by Cohen et al. is the first transgenic rat developed to challenge and compensate for these physiological relevance concerns of the mice models[26]. TgF344-AD expresses both the human APP and PS1 familial AD mutations, specifically the human APP Swedish (APP_{SW}) mutation and the Δ exon 9 human PS1 mutation (PS1ΔE9)[26]. Cohen et al. validated this animal cognitively and using immunohistochemistry. Significant cognitive impairments were observed at 15 months[26] (**Fig. 1.a.**). TgF344-AD also showed the full array of AD pathologies, including amyloidosis, gliosis, tauopathy, and neurodegeneration in an age-dependent manner, with amyloid-beta 42 and tau burden presenting as early as 6 months *in vivo*[26] (**Fig. 1. b-c**).

In vivo, TgF344 is a more physiologically relevant model than the more widely used mouse models, as it adequately recapitulates the full scope of pathologies of AD where the mouse models fail (**Fig. 1**). However, this novel AD rat model has yet to be modeled *in vitro*. For this thesis, we explore the application of the TgF344-AD rat line in our 3D primary cortical culture model.

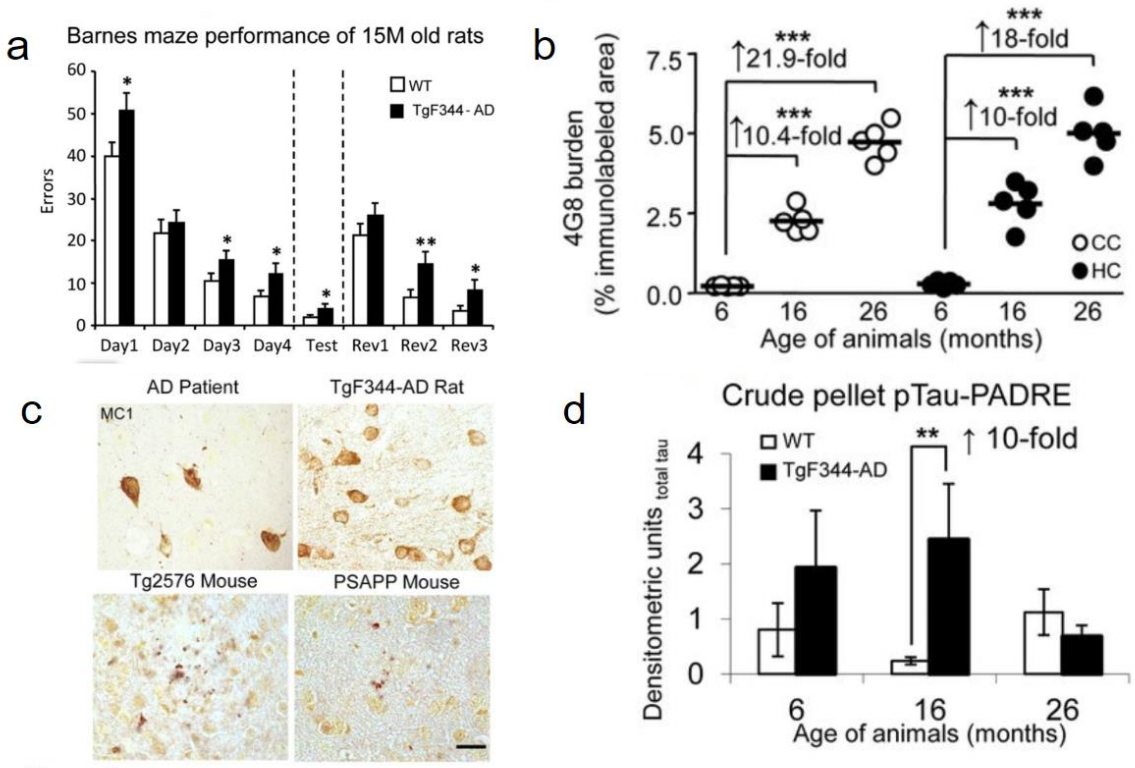

Figure 1

a , At 15 months, the TgF344-AD rat made significantly more errors in the barne maze than the WT counterparts in learning and reversal phases of the task (*p<0.05, **p<0.01). **b**, TgF344-AD rats exhibited an significant, age-dependant increase in amyloid-beta burden in both the Cerebral Cortex (CC) and Hippocampal Cortex (HC). **c**, Comparison of tauopathy in AD patients, Tg2576 mice , PSAPP mice, and TgF344-AD rat. **d**, Densitometric units of crude pellet pTau-PADRE show significant increase in TgF344-AD at 16 months compared to WT. Adapted from Cohen et al. 2013.[26]

Materials and Methods

Agarose Gel Formation

We followed the previously published protocol by Brown et al[30,47,48]. Agarose solution was first made by adding 50mL of sterile 1x Dulbecco's phosphate-buffered saline (DPBS; Sigma, Ref. #D1408) to 1g of sterilized agarose (Invitrogen, Ref. #16500). The solution was heated using a laboratory microwave until agarose went into solution and reached a rolling boil. Using a standard 24-well plate, a stainless-steel injection mold with 6 concentric holes was placed on a custom PLA lift over a single well. 1 mL of the boiling agarose solution was then injected into the well through the mold (**Fig. 2**). Leaving the mold in the well, the plate was placed on an ice pack,

allowing ample time to cool and solidify (roughly 7-8 minutes). Once cooled, excess agarose was scraped out of the injection mold using a sterilized stainless-steel rod, and the PLA lift-injection mold unit was gently removed (**Fig. 2**). An agarose-molded microwell consisting of an inner well with 6 concentric pegs remained. The agarose-molded microwells were then hydrated with Cell Culture Media (CCM) consisting of 48.4 mL Neurobasal-A (with phenol-red GIBCO, Ref. #10888-022; without phenol-red GIBCO, Ref. #12349-015), 0.125 mL GlutaMAX (GIBCO, Ref. #35050-61), 0.5 mL Penicillin Streptomycin, and 1 mL of 1xB-27 supplement (GIBCO, Ref. #17504-044), and stored in a 37°C incubator until seeding.

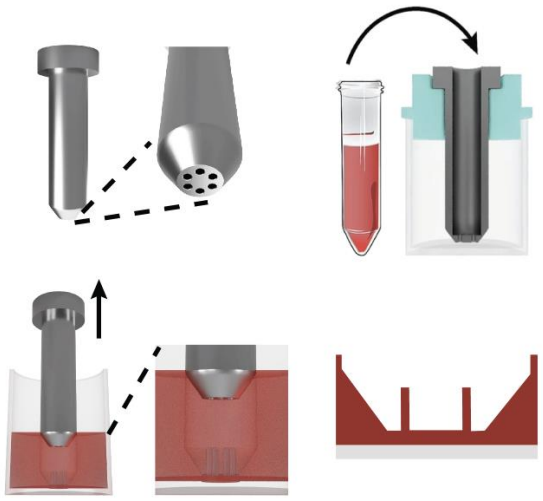

Figure 2
The stainless-steel injection mold is place within a PLA lift over a well. Hot agarose is injected through the mold, and allowed to cool, after which it is removed. Leaving behind 6 pegs, creating the agarose-micro feature for tissue seeding and formation. Adapted from Brown et al. 2023 [47]

Healthy Tissue

Primary Tissue Dissociation and 'Microtissue' Assembly: We used the protocol previously published by Brown et al[30,47,48] that was originally adapted from the Diane Hoffman-Kim Lab here at Brown University for the formation of primary cortical spheroids[28]. P0-1 Sprague Dawley rat pups were collected and sexed to ensure equal use of males and females. All animals were handled and euthanized in accordance with approved Institutional Animal Care and Use Committee (IACUC) protocols. Pups were anesthetized by hypothermia prior to euthanasia and

brains were carefully removed and placed in chilled Hibernate-A (Transnetyx Tissue Inc.) with B27-supplemented media (HA-B27) until time for further dissection (**Fig. 3**). Once all brains were collected, the dura was removed, and the cortices were excised (**Fig. 3**). Cortices were halved and cut into smaller pieces and added to a ~3mL Papain (Transnetyx Tissue Inc.) and Hibernate-A minus $CaCl_2$ (Transnetyx Tissue Inc., Ref. #020824) solution to be enzymatically dissociated into a single-cell suspension (**Fig. 3**). The cortices-Papain solution was then placed in a 30°C water bath for 30 minutes and inverted every 5 minutes to facilitate dissociation. After incubation, the supernatant was removed, and the pellet was resuspended in 2 mL of warm HA-B27. The 2 mL single-cell suspension was then added over a 40 µm filter and washed with 6 mL of HA-B27. The filtered solution was added to a 15 mL conical and centrifuged at 150g for 5 minutes. After centrifugation, the supernatant was removed and 2 mL of warm CCM was added to resuspend the solution. The CCM single-cell suspension was added over the top of a 40µm filter and washed with 6 mL of warm CCM. The filtered solution was transferred to a 15 mL conical and centrifuged at 150g for 5 minutes. This step was then repeated once more.

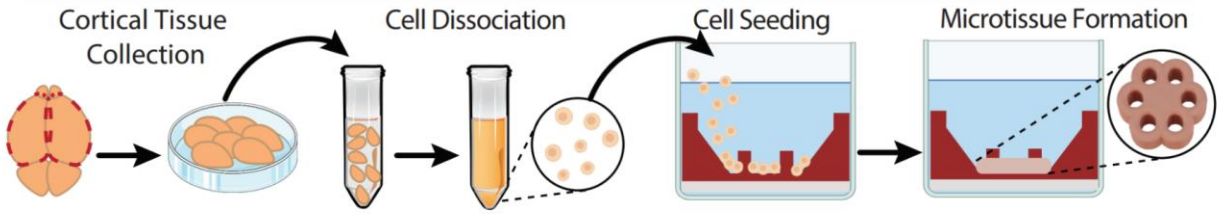

Figure 3
Cortices are dissected and dissociated into a single-cell suspension. Then they are subsequently seeded into the agarose micro-feature, where innate self-assembly forces result in 3D 'microtissue' formation. Adapted from Atherton et al. 2021 and Brown et al. 2023 [30,47]

After the third and final filter step, the remaining supernatant was removed, and 5 mL of warm CCM was added to resuspend the pellet. Cell count was assessed using a hemocytometer and Trypan Blue (BioRad, Ref. #1450013), in which 10 µL of the 1:8 counting dilution (5 µL of single cell suspension, 15 µL of supernatant, and 20 µL of Trypan Blue) were added to the hemocytometer. Before seeding, all the CCM in the agarose mold was removed, including the

innermost well. The seeding density was 2.9 x 10^6 cells per gel, and 10 µL of the single-cell suspension was added to a single well (**Fig. 3**). After seeding, the plate was placed in the incubator at 37°C for 25 to 30 minutes before adding media. Once cells were "set," 1 mL of CCM was carefully added back to the well over the top of the freshly seeded cells.

In the first 24 hours after seeing, cells self-assemble and start to contract inward toward the center of the well, creating a trampoline shape. After the first 24 hours, CCM was replaced. Subsequent media changes occurred every other day or on a Monday, Wednesday, and Friday schedule.

APP/PSEN 1 Tissues

Breeding: All animal handling and procedures were in accordance with approved Brown IACUC protocols. A male TgF344-AD rat, heterozygous for both APP/PSEN1 mutations, and two female wild-type (WT) Fisher 344 (F344) rats were ordered and placed in group housing in the CARE facility. The first breeder pair was set once the female reached 8 weeks old, and the pair was observed for the initial 5 minutes after introduction to monitor for signs of aggression. After the observation period, the animals were kept together for 2 weeks, after which they were separated, and the female was continually monitored for pups. After the first litter, these pups were left until the point of weaning, 21 days; at this point, males and females were separated, and ear punches were performed, both for genotyping and identification. Ear punches were sent to Transnetyx for initial genotype to subsequently select two APP/PS1 positive males for future breeding. The TgF344-AD male alternated breeding with the two female WT F344 rats until the younger males reached breeding age (6 weeks). At this point, the younger males alternated with the WT F344 females. All litters following the initial litter were allocated to 3D primary cortical culture.

DNA Extraction: We adapted a rapid genotyping protocol from the Qiagen DNeasy Blood & Tissue Kit (Qiagen, Ref. #69504) and from Professor Eric Morrow's Lab (Center for Translational Neuroscience, Brown University) to process neonatal tail snips for DNA extraction and subsequent PCR to confirm transgene expression in littermates. All Qiagen-provided solutions

were prepped following product instructions. P0-1 pups were collected, labeled with a number (pup ID), and tail snips 0.4-0.6 cm were collected and placed in a 1.5 mL microcentrifuge tube with corresponding pup ID. Brown University IACUC protocols approved all animal handling and procedures. After tail snips, pressure was placed on the site of the cut to top bleeding, and pups were returned to the container and placed on a heating pad until time to start the remainder of the dissociation protocol. 180 µL of ATL buffer (Qiagen 69504, Mat. #1063369) and 20 µL of Proteinase K (Qiagen 69504, Mat. #1014023) were added to 1.5 mL microcentrifuge tubes with tail snips, the solution was vortexed and then incubated in a water bath at 56°C until completely lysed. The solution was vortexed occasionally to aid in tissue lysis. Once the tissue was completely lysed, 200 µL of the AL buffer (Qiagen 69504, Mat. #1014594) was added, and the solution was vortexed before returning to the 56°C water bath for an additional 10 minutes. Then 200 µL of 100% EtOH was added, and the solution was vortexed and pipetted into the DNeasy Mini Spin Column within a 2 mL collection tube and centrifuged at 5000 rpm for 2 minutes. The flow through was discarded, the spin column was placed in a new 2 mL collection tube, and 500 µL of AW1 buffer (Qiagen 69504, Mat. #1014790) was added. The solutions were centrifuged at 5000 rpm for 2 minutes, and the whole AW1 addition and centrifugation step was repeated. Next, the spin column was removed and placed in a new 2 mL collection tube, after which 500 µL AW2 buffer (Qiagen 69504, Mat. #1014592) was added and centrifuged at 5000 rpm for 9 minutes. The process of adding AW2 buffer and centrifugation was repeated once more. The spin column was removed and placed in another 2 mL centrifuge tube, and 200 µL of AE buffer (Qiagen 69504, Mat. #1014572) was added to the spin column to elute the DNA. The solution was incubated at room temperature for 1 minute and then centrifuged for 2 minutes at 5000 rpm.

Genotyping: Genotyping was done using PCR and Gel Electrophoresis, detecting APP-positive genotypes. For the PCR, the master mix was created using 12.5 µL of GoTaq (Promega, Ref. #M513B), 0.5 µL mPRP F (IDT, Ref. #403901546), 0.5 µL mPRP R (IDT, Ref. #403901547), 0.5 µL APP F (IDT, Ref. #403901548), 2 µL of extracted DNA, and 9 µL of NucFree H_2O (Promega,

Ref. #P119A), reaching a total of 25 µL per sample. The PCR cycle parameters were 4 minutes at 95°C, 30 seconds at 94°C, followed by 30 seconds at 58°C and 1 minute at 72°C. This cycle was repeated for a total of thirty-five cycles. Then followed by 7 minutes at 72°C and ended at 4°C. 20 µL of solution was loaded onto the E-Gel (Invitrogen, Ref. #A42347)l, consisting of 10 µL of E-Gel loading buffer (Invitrogen, Ref. #10482055) and 10 µL of DNA solution, per sample. 20 µL of the DNA ladder (Invitrogen, Ref. #10488091) was loaded on either end of the gel, and 20 µL sample loading buffer was added to all empty wells.

The E-gel was run using the PowerSnap Device on the EGel Double Comb setting for 13 minutes, then extended to 15 minutes. The image was then taken using the PowerSnap device. To identify whether APP-positive or negative, APP-negative has a single, thick line at 799 bp, while APP-positive has a band at 400 bp and 799 bp.

Tissue Dissociation and 'Microtissue' Assembly: After pups were genotyped, they were anesthetized by hypothermia prior to euthanasia and separated between APP-positive and APP-negative. Two concurrent tissue dissociations were performed, one for APP-positive and one for APP-negative, following the same protocols for healthy tissue dissociation. After full dissociation and cell counting, the APP-positive and negative cells were seeded onto either different plates or the same plate, depending on the number of tissues, and labeled. Tissues were then fed carefully, using different tips, and supernatants were collected starting at a day *in vitro* (DIV) 6 until the fix date.

Tissue Fixation [47]

A 4% paraformaldehyde 8% sucrose solution was made by combining 4g of sucrose, 5 mL of formalin, and 45 mL of 1 x DPBS. On a predetermined day *in vitro* (DIV 2, 7, 28, 60), plates were removed from the incubator, and 1 mL of the 4% paraformaldehyde 8% sucrose solution was added to each well. The tissues stayed in solution for a minimum of 2 hours. The tissues were subsequently washed three additional times in 1 x DPBS for 2-hour increments. Tissues were then removed from the gels by excising the inner well from the main gel and then placing

the inner gel containing the tissue in 1 x DPBS on a hot plate at 200°C. As the gel melted, the tissue was removed from the agarose scaffold. Once released, the tissue was immediately removed and placed in a 48-well plate. 1 x DPBS was added to keep tissues hydrated and stored at 4°C until it was time to start the immunohistochemistry (IHC) process.

Immunohistochemistry (IHC)

First, a blocking solution was created using 8.9 mL of 1xDPBS, 0.1 mL of Triton X-100 (Sigma, Ref#T8787), 1 mL of Normal Goat Serum (NGS; Jackson ImmunoResearch, Ref. #005-000-121), and 0.4 g of Bovine Serum Albumin (BSA; Sigma, Ref. #A7030-100G). The blocking solution was allowed ample time to go into a homogenous solution and to chill at 4 °C. Tissues were then organized on a 48-well plastic plate based on the assay and future primary antibody conditions. 500 µL of the blocking solution was subsequently added to each well, and the plate was placed on a shaker at a speed of 3 for 2 hours. Next, the primary antibody cocktails were made with 300 µL of block per well, which depended on the conditions/cell of interest for a particular tissue (**Table 1**). After the primary cocktail addition, the plate was wrapped in parafilm and left on the shaker at a speed of 3 overnight.

Day 2 of IHC started with removing the primary antibody cocktail, placing them in labeled 1.5 mL microcentrifuge tubes, and storing them for further use. These cocktails could be used up to 3 times. PBT solution was made by adding 0.1 mL of Triton X-100 to 50 mL of DPBS. 500 µL of PBT was then added to each well and returned to the shaker on speed for 2 hours. After that, the PBT was replaced, and the plate was returned to the shaker for 2 hours. Then, the PBT was replaced with 500 µL of blocking solution, and the plate was returned to the shaker for 2 more hours. While the plate was incubating in the block, the secondary cocktail was made, which consisted of 300 µL of block per well and secondary antibodies (**Table 1**) at a concentration of 1:800. After 2 hours, the block was replaced with the secondary antibody cocktail, wrapped in parafilm, and covered with tin foil, before the plate was returned to the shaker overnight. Day 3 started with the removal and discard of the secondary antibody cocktails, followed by four

consecutive 1-hour washes with PBT, and ending with a 1-hour wash with DAPI (**Table 1**). 300 µL of DAPI solution was added to each well, with a DAPI concentration of 1:1000. Following the 1-hour incubation with DAPI, the solution was removed and replaced with 1 x DPS, after which the plate could be immediately imaged or stored at 4 °C until imaging session.

Imaging

Samples were removed from a 48-well plate and plated onto a glass bottom petri dish (Mattek, Ref. #P35G-1.5-14-C) with minimal 1 x DPBS. Images were taken using the Olympus FV3000 Confocal Microscope, using resonant and sequential scanning to collect volumetric image data. Images with magnification of 10x, 30x, and 30x with a digital zoom (3z) were taken for each sample. Some tissues were flipped, and images were taken of both sides. All 30x 3z were taken in four quadrants and later stitched together using the FluoView software associated with the microscope. Observation methods were saved to standardize the fluorescence intensity across samples. However, there was usually some manipulation and variation from tissue to tissue.

Analysis

Initial Image Processing: OIR images were imported into ImageJ, where they were initially processed. The multi-channel images were split, and channel 3 was turned magenta for easier viewing. First, volumetric images were compressed into 2D images by taking the maximum fluorescence intensity at each pixel, generating a 2D maximum-intensity image. A scale bar was input. Then, images were saved as TIFF and PNG for later analysis.

Cell Counting: The 30x magnification, plus 3 zoom stitched images, were used for cell counting. These images were input into ImageJ and the channels were split. Channel 3 and Channel 1 colors were changed to Magenta to aid in visualization and contrast. A designated region of interest (ROI; 186.17 x 199.98 µm) with a designated and constant position encompassing the center of the tissue was placed in each hyperstack for every stitched image. To eliminate background areas or regions not included in the ROI, the ROI and the hyperstack were duplicated.

This was done for every channel of the image. Next, the DAPI channel (C=0) was merged with each corresponding channel of interest. Then, the volumetric images, or z-stacks, were parsed through, slice by slice, and using the multi-point selection tool with “Labels” and “show on all slices” enabled, cell bodies with DAPI overlay were tagged. This process was repeated twice per sample, with average n=6.2 for div 2 samples, n=6.8 for div 7 samples, n=6.2 for div 28 samples, and n=6 for div 60 per cell type across 5 biological replicates for WT Sprague Dawley rat tissues. The final two counts per sample were averaged and input into GraphPad Prism. For the TgF344-AD (Fisher rat) cultures, there was an n=2 for astrocyte and neuronal nuclei cell counts and an n=1 for microglia, oligodendrocyte progenitor cells (OPCs), and neural progenitor cells. TgF344-AD counts were limited to a single day in culture, DIV 46. A simple One-Way ANOVA was performed, with a Tukey test for multiple comparisons.

Mean Fluorescence Intensity: The maximum intensity TIFFs that were previously processed were opened in ImageJ. Then, the image was transformed into an RGB Color Image (Image>Type>RGB Color). Followed by the transformation into a 16-bit image, turning the image grayscale (Image>Type>16-bit). The image was measured to calculate the mean fluorescence intensity (Analyze>Measure), with the measurements set to include the “Mean gray value.” These measurements were then input into an Excel spreadsheet and were grouped by DIV (2, 7, 28, 60) or the single DIV 46 for TgF344-AD cultures. Next, these measurements were input into GraphPad Prism, where a One-Way ANOVA with multiple comparisons was run, and the results were graphed. There was an average of n=13 for Sprague Dawley WT tissues, and in the TgF344-AD cultures, the n=2 per condition.

2D Sholl Analysis: Sholl analysis is often used as a metric to evaluate the complexity of microglia morphology by counting the number of intersections within concentric rings extending around the centroid. The Microglia Segmentation and Tracking ImageJ plugin was used for 2D Microglia Sholl Analysis[61,62]. Upon opening the plugin (Plugins>Microglia>New Microglia Segmentation and Tracking), user-specific parameters were set for Intensity Threshold (1.50), Minimal cell size

(160), and Maximal cell skeleton length (80). The Intensity threshold remained unchanged from the plug-in default; however, the minimal cell size and maximal cell skeleton length were manually adjusted based on measurements and approximations from the previously saved TIFF Maximum Projection images. Following the parameter inputs, the image of interest was input under the "intensity image time series" prompt, and the output directory was selected. Separate files were set up per sample and subsequently per skeleton within a sample to minimize confusion. After the plugin was completed, a grayscale intensity image and labeled-masked image were generated (**Fig. 4. a-b**). These two files were saved in the file corresponding to their sample ID.

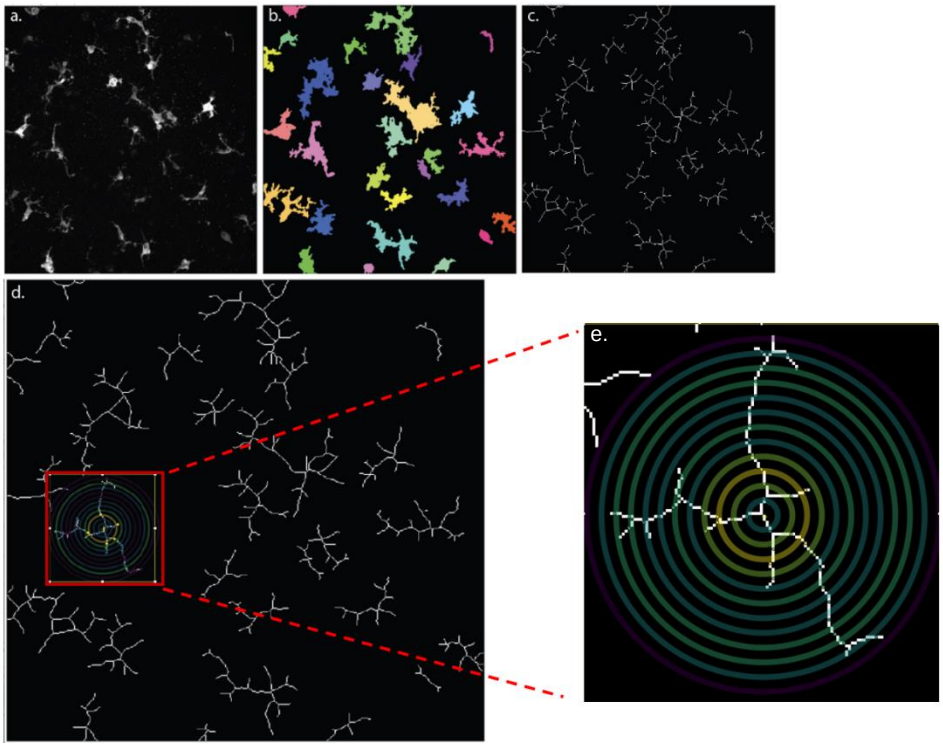

Figure 4
Depiction of the process for 2D sholl analysis using Microglia morphology ImageJ[61] plugin and SNT Sholl Analysis plugin[62]. **a**, Intensity image of 30x magnification maximum projection; **b**, Segmented image; **c**, Skeletonized image; **d-e**, Sholl analysis. Spheroid cells were skeletonized to have 3-4 initial branches.

With the intensity images and the labeled image, the second portion of the "Microglia Morphometry" plugin was used (Plugin>Microglia>Measure Microglia Morphometry)[61]. Upon opening this program, the intensity image from the previous step was input in the "Intensity image

time series," and the labeled-masked image was input under the "Label mask time series." The output directory was selected to be the same as the previous step, with the file being sample-specific. The resulting outputs were annotations of the intensities, in which each center of mass was identified, and the other was a skeletonized image of the intensities (**Fig. 5.c**).

Folders associated with each skeleton to be analyzed were created for an n=3 per sample. The skeletonized image was opened in ImageJ, and the ROI manager was used to select a skeleton for further analysis. Skeletons were selected by comparing the skeletonized image with the maximum projection image of the microglia overlaid with DAPI. This was done to ensure one cell was being counted and to determine the centroid for the Sholl analysis. Cells with merged or overlapping skeletons were ineligible for analysis. The SNT plugin from Neuroanatomy was opened, and the Sholl analysis>Sholl Analysis (Image) was selected[62]. This opened a new window to determine Sholl Analysis parameters (**Fig. 5.d-e**). First, the center from the active ROI was set and adjusted so it overlaid the nucleus (DAPI and Iba-1) and the "preview" option was selected to facilitate the adjustment of the following parameters. The start radius and step size were determined to be 5 µm and maintained constant across all skeletons analyzed; however, the end radius was customized to the skeleton, depending on the length of its extensions and its proximity to neighboring cells, the average radius used was 30 ɥm for div 2 samples and 60 ɥm for div 28 samples in WT Sprague Dawley microtissues, and 60 ɥm for the DIV 46 TgF344-AD microtissues. In addition, only full shells were used for this analysis. The remaining parameters were unchanged from the default, 'infer from starting radius,' 'best fitting degree,' 'automatically choose,' and 'default.' Finally, the outputs provided both linear and normalized plots and a detailed table and summary. The results were saved in the corresponding tissue and skeleton. This whole process was repeated for an n=3 across 3 biological replicates per time point in Sprague Dawley WT and for an n=3 across 1 biological replicate at DIV 46 in TgF344-AD microtissues.

The resulting information, radius, and number of intersections were input into GraphPad Prism under their corresponding DIV. A Two-Way ANOVA with multiple comparisons was performed.

Enzyme-linked immunosorbent assay (ELISA): Supernatants were collected for all TgF344-AD samples, both APP/PS1-positive and wild-type (WT), starting on day 6 *in vitro* and every subsequent feeding day (Monday, Wednesday, and Friday). Collected supernatants were put in labeled 1.5 mL microcentrifuge tubes corresponding to the sample ID and stored at -20°C. With cooperation from the Huang Lab (Laboratories for Molecular Medicine, Brown University), an ELISA was run on DIV 6 and DIV 28 WT and AD tissues (n=3 for both genotypes per time point) to test for the concentration Aβ-42, one of the amyloid fibrillary species associated with AD and the toxic AD plaque formation. Solutions were serially diluted to known concentration and a standard curve was generated to calculate the amount within the unknown samples. Two-way ANOVA with multiple comparisons was completed for statistical analysis.

Results

Nestin-positive neural progenitor numbers significantly decreased after day 7 in vitro: Across 60 days in culture for Sprague Dawley WT microtissues, with sampling at DIV 2, 7, 28, and 60, there was no significant change in cell numbers in Neun-positive neurons (p=0.3191) (**Fig. 5.**), Iba-1-positive microglia (p=0.0785, **Fig. 5**) and NG2-positive oligodendrocyte precursor cells (p=0.156, **Fig. 5**). There was a significant difference in the number of GFAP-astrocytes (p=0.0076; **Fig. 5**). Day *in vitro* 28 saw a peak number of astrocytes, significantly different from day 7 (p=0.0057) and day 60 (p=0.0394). Nestin-positive neural progenitor cells observed a significant variation in cell counts across the 60 days in culture (p<0.0001; **Fig. 5**). The differences in neural progenitor cells significantly change across each time point (DIV 2,7,28,60) with the significant decrease in cell numbers observed between day 7 and 28 (p<0.0001) and day 7 and 60 (p<0.0001).

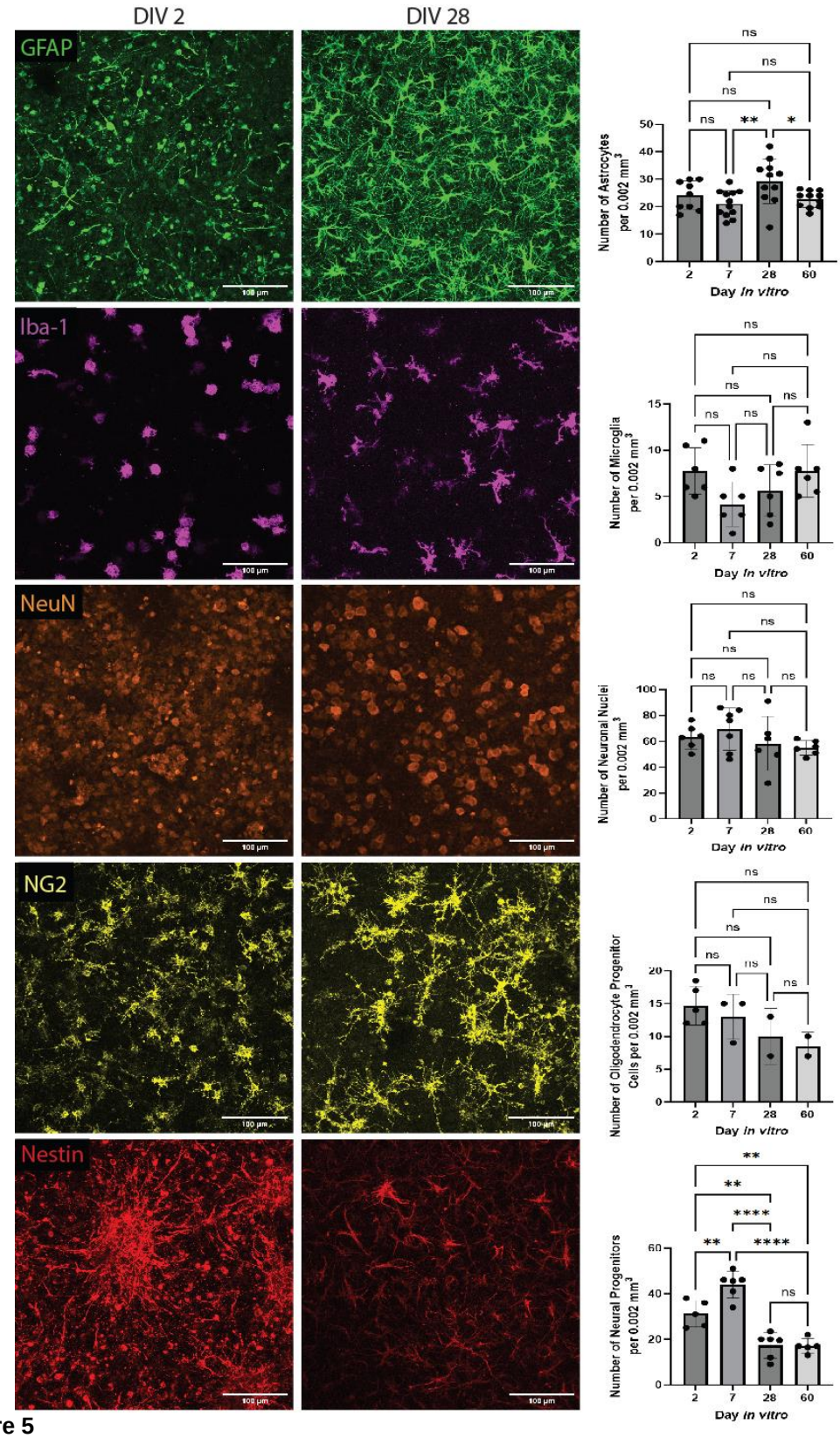

Figure 5

30x magnification maximum projections of astrocytes (GFAP, green), microglia (iba-1, magenta), neuronal nuclei (NeuN, orange), oligodendrocyte progenitor cells (OPCs; NG2, yellow), neural progenitors (Nestin, red) at DIV 2 and DIV 28. Corresponding cell counts per 0.002mm^3 at DIV 2, 7, 28, and 60 (* $p \leq 0.05$, ** $p \leq 0.01$, *** $p \leq 0.001$, **** $p \leq 0.0001$). Scale bar is 100 µm.

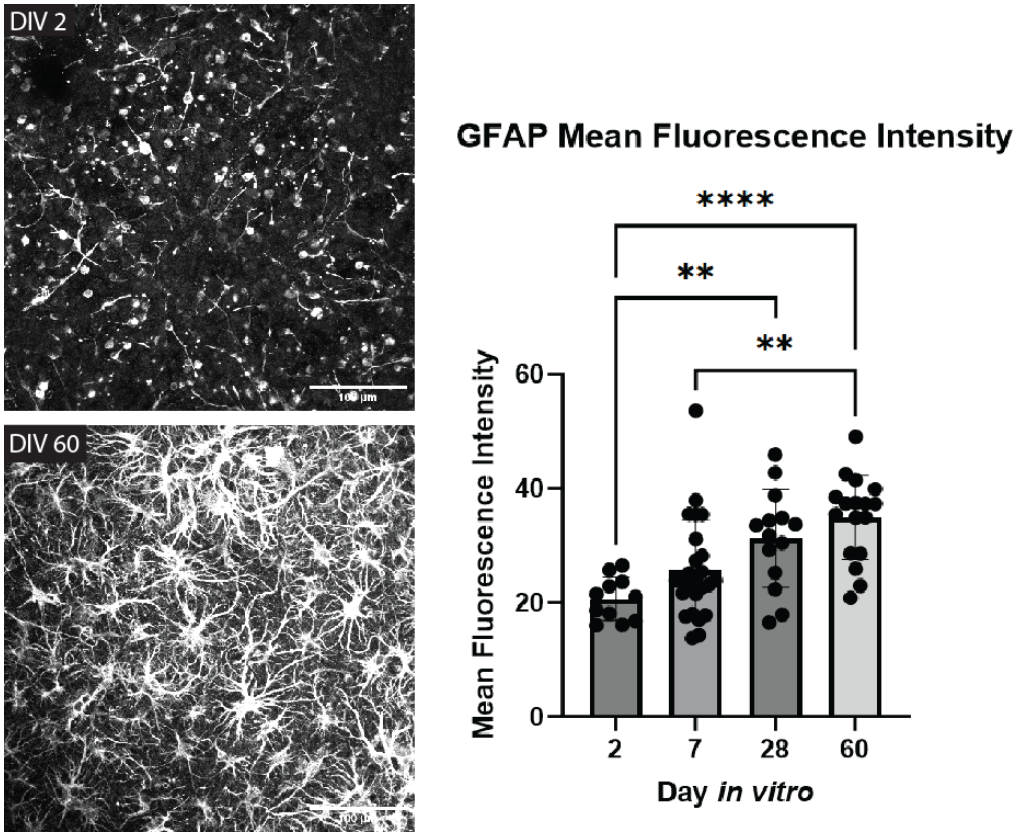

Figure 6
Left, shows greyscale, maximum projection images of GFAP-positive astrocytes at DIV 2 and DIV 60 that were later measured for mean fluorescence intensity. Right, shows graph depicting mean fluorescence at DIV 2, 7, 28, and 60 (* $p \leq 0.05$, ** $p \leq 0.01$, *** $p \leq 0.001$, **** $p \leq 0.0001$). Scale bar 100 µm

Mean Immunofluorescence Intensity increased in GFAP-positive astrocytes across 60 days in culture: The mean fluorescence intensity of GFAP-positive astrocytes significantly increased across the 60 days in culture ($p<0.0001$; **Fig. 6**) in Sprague Dawley WT cultures. From day 2 to day 60, there was a significant increase in GFAP mean fluorescence intensity ($p<0.0001$). Other significant increases include days 2 to 28 ($p=0.0066$) and days 7 to 60 ($p=0.002$). Changes between days 2 and 7, 7 and 28, and 28 and 60 were not statistically significant.

Microglia exhibited more extended ramifications and greater branching in older samples: In the microglia 2D Sholl analysis comparing Sprague Dawley WT day 2 samples and day 28 samples, there was a significant difference in the number of intersections between the 15 µm radius through the 55 µm ($p<0.0001$; **Fig. 7**). The differences in the number of intersections from

a radius of 15 µm through 45 µm had an extremely significant difference, with a p<0.0001. While the difference at radius at 50 µm had a significance of p= 0.0035, and 55 µm had a p=0.0211. The shorter radii of 5 µm and 10 µm and the furthest radius of 60 µm did not exhibit significant differences.

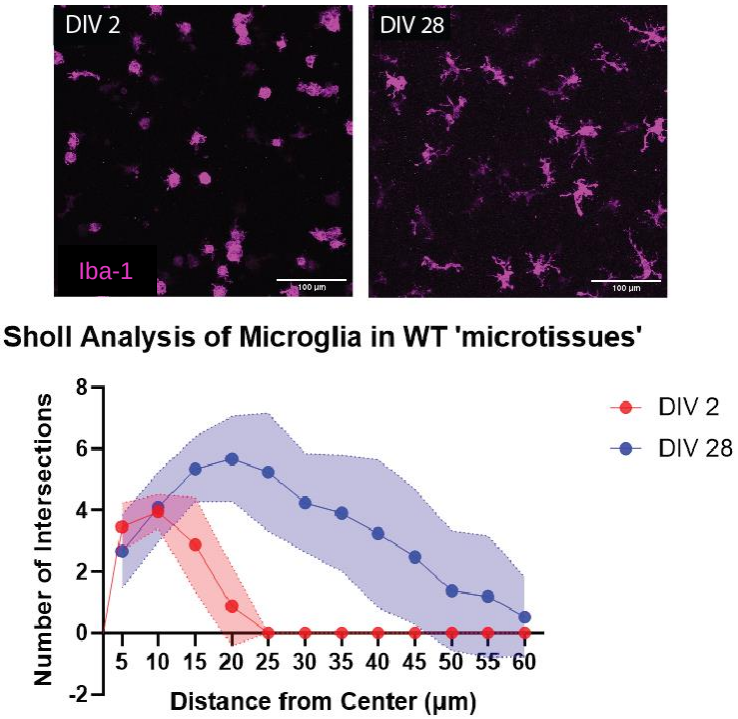

Figure 7
2D maximum projection sholl analysis of WT iba-1-positive microglia (magenta) at DIV 2 and DIV28. DIV 28 had significantly more intersections at radii 15 µm through 45 µm (p<0.0001), 50 µm (p=0.0035), and 55 µm (p=0.0211). Scale bar 100 µm.

Distinct morphological changes across 60 days in culture and ECM presence: The extracellular matrix (ECM), including Collagen IV and Laminin, exhibited positive immunoreactivity at various time points in culture (**Supp. Fig. 1**). Other ECM markers, like the Lectin of *Wisteria floribunda* (WFA) staining for perineuronal nets, also showed positive immunoreactivity, indicative of their presence (**Supp. Fig. 1**). The axonal markers of Beta-3 Tubulin (B3T) and MAP2 exhibited positive immunoreactivity (**Supp. Fig. 1**). Concerning oligodendrocytes, mature oligodendrocyte staining with O1 exhibited positive immunoreactivity with Myelin Basic Protein (MBP) overlap. However, they lacked clear ramifications and

myelinating processes. Staining with NG2 highlighted the OPC population's extensions and phenotypes within the microtissue (**Fig.5**). There was also a distinct morphological transformation across the microglia, neural progenitor, and astrocyte populations (**Fig.5**). The day 2 microglia appear more ameboid and spheroid than their day 28 and day 60 counterparts, which appear more ramified. Day 2 and 7 astrocytes appear more spheroid, some exhibiting a single extension, while the later time points have extensive ramifications and a “bushy” appearance. Nestin-positive cells appear in clusters on day 2 and appear more diffuse throughout the tissue at day 7 (**Fig. 5,8.a-b**). By day 28, the Nestin-positive cells resemble closely to astrocyte morphology, looking more “bushy” (**Fig.5**). On day 2, the Nestin-positive and GFAP-positive cells appear to populate contrasting spaces within the tissue, creating a mosaic (**Fig. 8**).

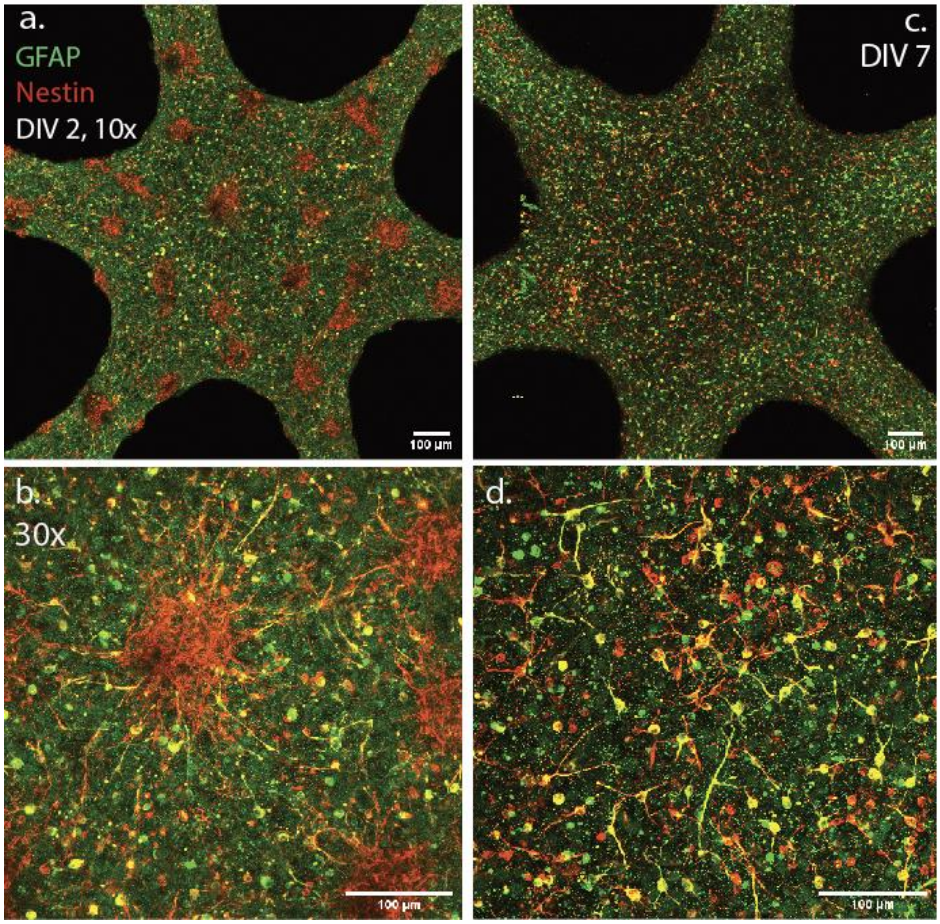

Figure 8
Maximum projections and overlayed confocal images (**a,c** 10x, **b,d** 30x) of neural progenitors (Nestin, red) and astrocytes (GFAP, green), with overlapping signals in yellow. **a,c** DIV 2, **d,e** DIV 7. Scale bar 100 µm.

Amyloid-β 42 concentrations were significantly greater in APP/PS1-positive cultures than in wild-type cultures: ELISA analysis of supernatants showed significant increases in the concentration of Aβ-42 between APP/PS1-positive cultures and WT cultures at both day 6 (p=0.0002) and day 28 (p<0.0001) *in vitro* (**Fig. 9.c**). There was also a significant increase in the concentration of Aβ-42 between day 6 and day 28 of the AD tissues (p=0.0004, **Fig. 9.c**).

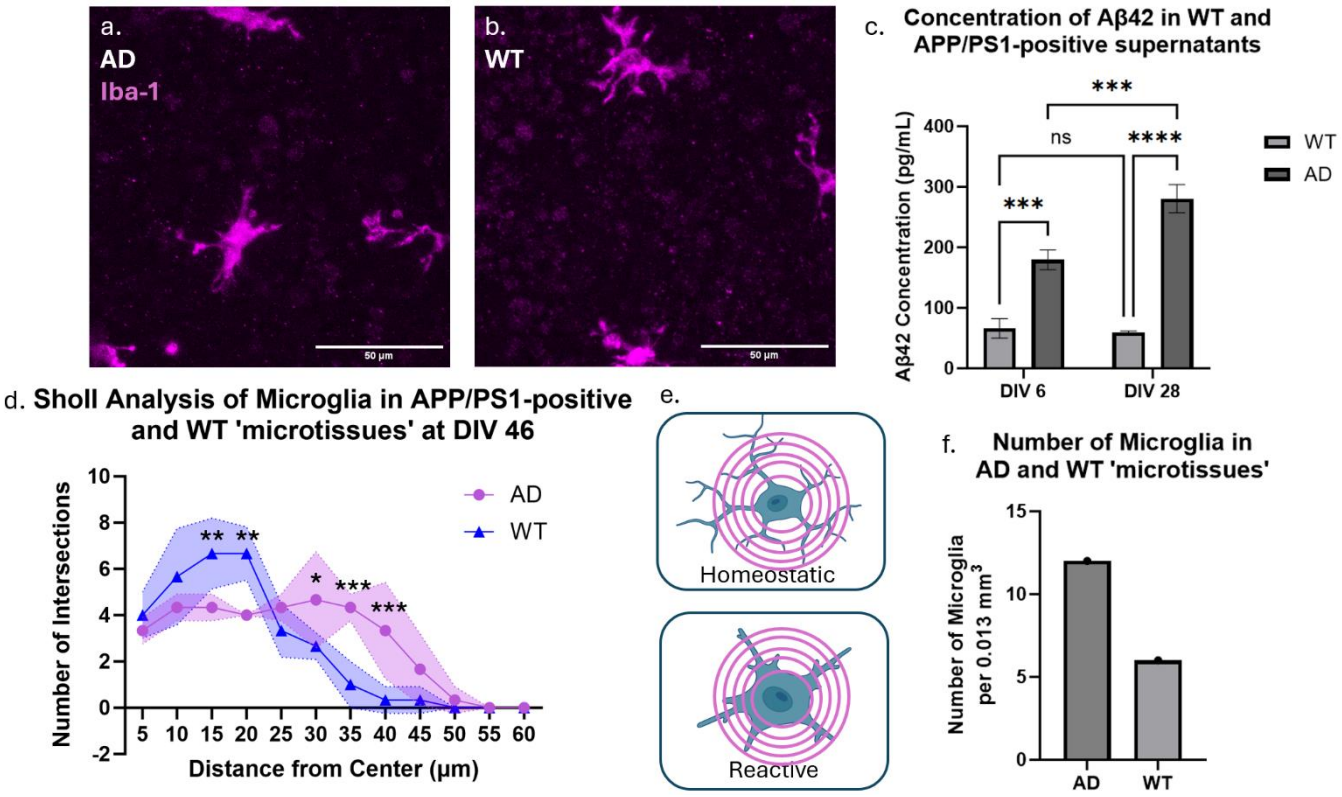

Figure 9

a-b, Maximum projections of 30x 3 zoom confocal microscopy images of iba-1- positive microglia (magenta) in AD and WT tissues on DIV 46. **c**, ELISA results for Aβ42 concentration in AD and WT tissues at DIV 46. **d,** 2D sholl analysis of iba-1-positive microglia in AD and WT DIV 46 cultures. **e,** rendering of 2D sholl analysis on homeostatic and reactive microglia. **f,** cell counts for microglia in AD and WT tissues at DIV 46 (n=1 per condition). (* p ≤ 0.05, ** p ≤ 0.01, *** p ≤ 0.001, **** p ≤ 0.0001). Scale bar is 50 µm.

2D Sholl analysis revealed significant microglial morphological differences between AD and WT tissues: At 15 µm and 20 µm radii, the microglia of the Fisher wild-type tissues had significantly more intersections than the microglia of the AD tissues (15 µm, p=0.0197; 20 µm, p=0.0197; **Fig. 9.d**). The microglia of the AD tissues had significantly more intersections at radii

30 μm (AD to WT p=0.0211), 35 μm (AD to WT p=0.0027) and 40 μm (AD to WT p=0.0075) than WT tissues (**Fig. 9.d**).

No significant difference in cell counts or mean fluorescent intensity was observed between AD and WT tissues: Cell counts did not show any significant changes in the number of astrocytes, neuronal nuclei, microglia, OPCs, and neural progenitors between AD and WT tissues (**Fig. 9.f, 10.c)**. However, there appears to be a difference in neural progenitors, with WT tissues having more than AD tissues; significance is not determined. There were also slightly more astrocytes in AD cultures than in WT cultures, while there were slightly fewer OPCs and neuronal nuclei in AD tissues than in WT tissues, significance not determined. AD tissues had more microglia than WT tissues; however, with only an n=1, significance cannot be determined (**Fig. 9.f**).

There was no significant difference in GFAP-astrocyte mean fluorescence intensity across AD and WT tissues (**Fig. 10.b**). However, the wild-type tissues appeared to have a slightly greater GFAP-astrocyte mean fluorescence intensity than the AD tissues.

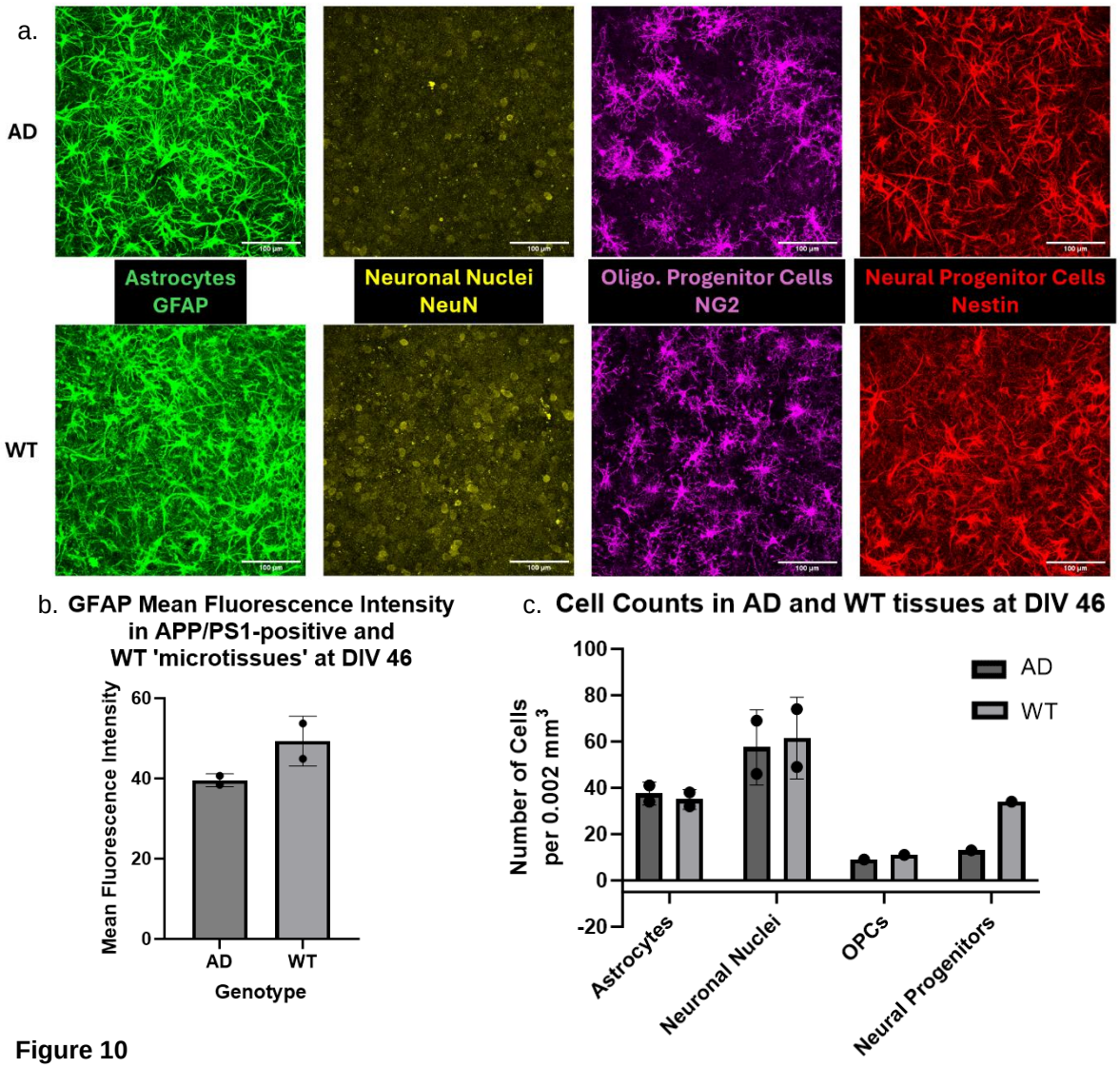

Figure 10

a, 30x magnification maximum projection confocal microscopy images of astrocytes (GFAP, green), neuronal nuclei (NeuN, yellow), oligodendrocyte progenitor cells (OPCs; NG2, magenta), and neural progenitors (Nestin, red) at DIV 46. The top row depicts AD tissues, bottom row depicts WT tissues. **b,** GFAP-astrocyte mean fluorescent intensity at DIV 46 in AD and WT cultures (not significant, ns). **c**, Cell counts of astrocytes, neuronal nuclei, OPCs, and neural progenitors at DIV 46 in AD and WT tissues (ns). Scale bar is 100 μm.

Discussion

The use of 3D *in vitro* cell culture models has grown in recent years as researchers try to probe critical questions regarding molecular processes of disease in a physiologically relevant manner while maintaining a high level of throughput and reproducibility. These concerns are especially prevalent as they relate to the highly sensitive cortical environment and associated

neurological diseases such as Alzheimer's disease. Aimed at addressing these concerns as they relate to a cortical culture, we describe and further characterize a physiologically relevant scaffold-free 3D primary cortical culture model that maintains the operational benefits of *in vitro* models and explore its application as a means to study the cell-type specific interactions and mechanisms in Alzheimer's disease pathogenesis.

In our evaluation of Sprague Dawley wild-type 'microtissues,' we tracked multiple cell types over 60 days to observe cellular changes and establish a baseline before applying this system to an AD model. One of these observed cell types was neural progenitor cells labeled with Nestin. Nestin-positive cells exhibited a significant decrease in the number of cells expressing Nestin after day 7 *in vitro* (**Fig. 5**). In addition, at day 2, our cultures exhibit an almost inverse expression pattern between the rosette-like Nestin clusters and the diffuse GFAP signals, but at later time points, there is more overlap and, qualitatively, the later Nestin-positive cells appear more astrocyte-like (**Fig. 5, 8. a-b**). A potential explanation for this significant drop in Nestin-positive cells is the change in cell-type identity and behavior as the neural progenitors mature and differentiate in culture[63, 64]. However, the question remains regarding Nestin's apparent prolonged expression in astroglia and the subsequent overlap with GFAP-positive cells. New evidence suggests that the Nestin-positive/GFAP-negative cells are more indicative of neurogenesis and replication, while cells with overlapping signals may be arrested in development and no longer cycling[63].

GFAP-positive astrocytes also exhibited a significant change in cell numbers, with a significant peak at day 28. It's unclear as to why this may be and requires further investigation. While the other cell types of interest we evaluated did not show any significant changes in cell numbers, apparent morphological changes were observed. The astrocyte population matured from small cell bodies with only a few "tails" to bushy, mature astrocytes with complex extensions and ramifications (**Fig. 5**). As they matured, the overlapping processes of the astrocytes proved challenging for cell counting, so we used GFAP mean fluorescent intensity as a metric for GFAP-

astrocyte expression in our samples, which has been previously used to quantify GFAP-astrocyte populations[65,66]. The significant increase in GFAP mean fluorescent intensity over the 60 days indicates the changing morphology and maturation and, likely, differentiation of GFAP-positive astrocytes (**Fig. 6**).

Microglia also exhibited significant morphological changes throughout the 60 days in culture, as they became more ramified with more extensions. On day two, the microglia appear more ameboid, consistent with a more reactive state[67,68]. By days 28 and 60, the microglia became more ramified with an increased number of intersections and branches, as evidenced by the 2D Sholl analysis (**Fig. 7**). One hypothesis for this is that the physical dissociation process induces the reactive phenotype of the microglia, as observed DIV 2; however, once the cells are given time to settle in the microtissue, they relax into a more homeostatic state[67,68]. Interestingly, at DIV 7, very few, if any, iba-1-positive microglia are seen. This could suggest a changing expression pattern among the microglia at this time, where they are not widely expressing iba-1. Additionally, in the earlier time points, the iba-1 positive microglia tend to initially settle to one side of the tissue, which is when flipping the tissue is required for imaging; however, later, they are more diffuse throughout the tissue, suggesting a migration through the tissue.

Various other cell types were present within our 3D model; however, they were more challenging to quantify, namely, the varying ECM components, like Collagen IV and Laminin, and even the WFA for perineuronal nets (**Supp. Fig. 1).** While there was positive immunoreactivity to these components, further investigation is required to capture the full dynamics within our microtissues. However, the presence of these ECM components was expected. With the nature of primary cell culture, all original elements from tissue collection are included, meaning any endogenous ECM. In addition, the tissues' ability to self-assemble and contract and survive for 60 days without any additional scaffolding or serum is also evidence of the presence of endogenous ECM[40]. Other elements, like axons, were visible and dense, which is also expected

from the nature of primary cortical culture and due to the extensive presence of neuronal nuclei (**Fig. 5**).

We tested for oligodendrocytes using a variety of markers: NG2, O1, Olig2, and MBP (**Supp. Fig. 2**). We evaluated for both mature and immature/precursor oligodendrocytes. While each of these markers showed positive immunoreactivity, the only marker that revealed robust cell bodies and extensions was the NG2 antibody, which labeled OPCs (**Fig. 5**). In contrast, the mature marker O1 did not distinguish clear cell bodies with ramifications however it did co-express with MBP (myelin basic protein) (**Supp. Fig. 2**). MBP expression can often indicate mature oligodendrocytes as they are able to myelinate, so there is still a question as to why the O1 staining did not resemble myelinating oligodendrocytes with distinct ramifications as the OPCs did. This question requires further investigation. However, one theory is that the mature oligodendrocytes are missing some signaling cue, potentially vasculature, that is causing a stall in their development, resulting in abnormal staining[69-71]. This is a plausible explanation, as there are known links between oligodendrocyte development and their association with blood vessels[69-71]. Alternatively, another potential explanation is the size of the axons within our culture, as the wrapping of axons is essential for oligodendrocyte survival and maturation[73]. If the axons are too small, then the oligodendrocytes are unable to wrap around them, stalling maturation[73]. However, we do have robust numbers of ramified OPCs, so a stall is likely to occur after these cells can express MBP.

After we characterized the cellular diversity over the 60-day culture in the Sprague Dawley WT tissues, we applied the novel TgF344-AD rat line to this 3D model. All the AD samples were sourced from female pups in the assay by chance, while the WT cultures were separated into males and females. However, the male WT tissues largely failed to form, so the WT tissues were analyzed solely from female tissues. While we may decide to do mixed-sex samples in the future, this assay provided a unique opportunity to split the sexes and examine molecular changes solely in female AD cultures. This occurrence aligns with the clinical presentation of AD, in which two-

thirds of those diagnosed with AD are women[2]. In the future, we know that we can examine sex differences in disease and WT states, as we previously started in this study.

While there were no significant changes in GFAP-mean immunofluorescent intensity or cell counts in the AD versus WT cultures, we were limited by the number of samples, so it's unclear whether a larger sample size would render different results (**Fig. 9.f., 10.b-c**). However, there were observable, non-significant differences between cell counts in AD and WT cultures, specifically between neural progenitors and microglia. This result could be affected by a larger sample size, but an increased number of microglia in the AD tissue would be pathologically consistent with an elevated microglia response to neuroinflammation and AD, while fewer neural progenitors in the AD tissue aligns with the loss of neurogenesis pathology in AD.

There was a significant increase in the concentration of Aβ42 as early as day 6 *in vitro*, which grew by day 28 (**Fig. 9.c**). This evidence begins to present a potential timeline for molecular changes that occur before plaque and tangle onset. Even with a limited sample size, there were significant differences in microglial ramifications evident from the 2D Sholl analysis (**Fig. 9.d**). The Sholl analysis indicates that the WT culture has more ramified microglia in the shorter radii (more branch points and extensions closer to the cell body). In contrast, the microglia in the AD cultures appear to have significantly more branches or longer extensions further away from the cell body. This supports that there are significant morphological changes between AD and WT microglia. These changes could be a result of larger, more ameboid cell bodies in AD cultures indicative of a more reactive state, so we aren't counting their intersections beyond the cell body until a further distance when compared to the smaller cell body of a more homeostatic microglia. While we have yet to examine for the presence of AD pathological hallmarks, like amyloid-beta plaques and tau tangles, these results suggest that the elevated levels of Aβ42 in the microenvironment are initiating cellular and molecular changes prior to the onset of the hallmark pathological plaques and tangles observed in AD.

In conclusion, we have shown our 3D primary cortical culture model to be a dynamic, multicellular environment containing a wide array of endogenous cellular diversity and can be cultured for extended lengths of time without a scaffold or added serums. This model can also incorporate the use of transgenic animals, like TgF344-AD, for the application of Alzheimer's research, with the possibility of other disease states. To our knowledge, this was the first *in vitro* comparative study for the TgF344-AD rat model. In this thesis work, we observed molecular and cellular changes within this in vitro transgenic culture, indicating possible pathogenic features that predate the canonical protein aggregate pathologies. This model could produce more significant insights by expanding the sample size, extending cultures, and evaluating the occurrence of amyloid plaques and tau tangles. In addition, we could further probe the neuroinflammatory response by analyzing the secretions within these cultures by evaluating for the presence of inflammatory markers and cytokines and testing whether they correlated with the Aβ42 concentration. Additionally, this model has unique compatibility with longitudinal live imaging studies; in the future, we could implement these live imaging techniques to continuously monitor these cell populations for the duration of the TgF344-AD cultures. Ultimately, this thesis validates this 3D model's compatibility with transgenic cultures and shows that this model could be applied to answer more questions than the ones addressed in this thesis

Supplemental Figures

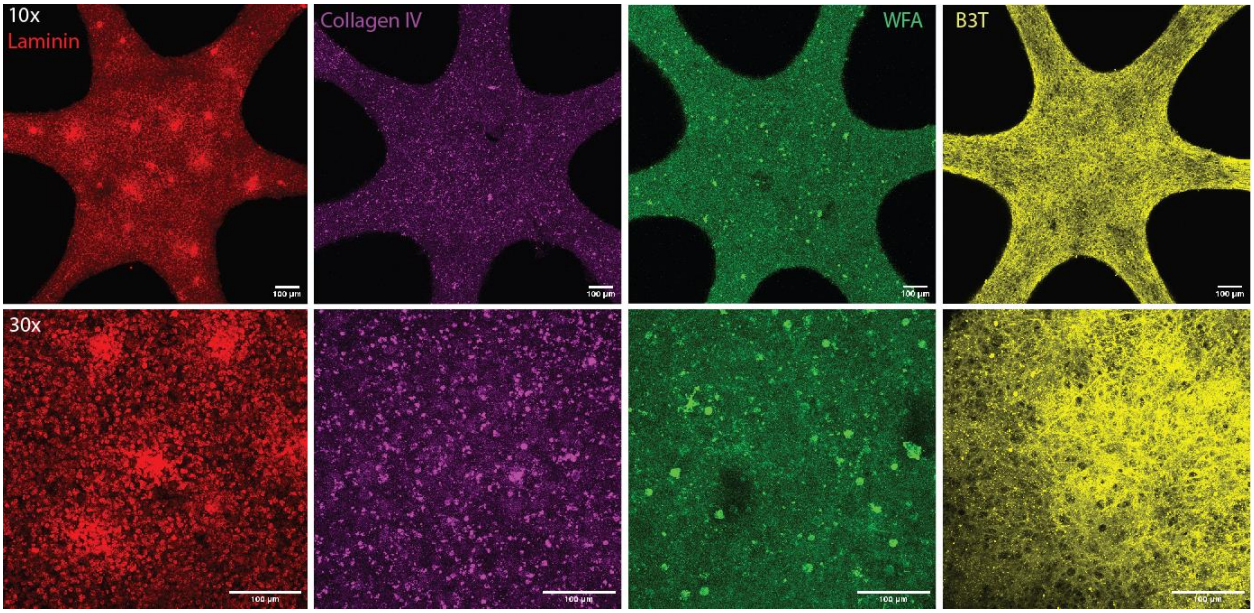

Supplemental Figure 1
ECM components Laminin (red), Collagen IV (magenta), and WFA (green); axonal marker B3T (yellow). DIV 28 10x magnification (top row), 30x magnification (bottom row). Scale bar 100 μm.

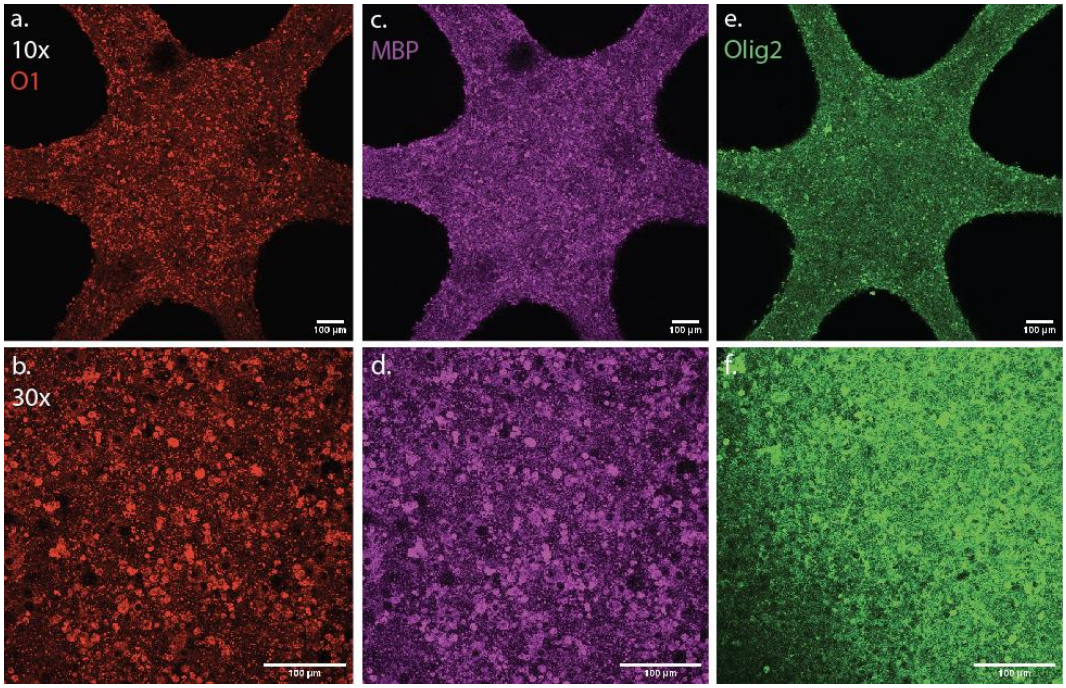

Supplemental Figure 2
Varying oligodendrocyte markers at DIV 28, O1 (**a,b**; red), MBP (**c,d**; magenta), and Olig2 (**e**,f; green). All maximum projections, **a,c,e** 10x magnification; **b,d,f** 30x magnification. Scale bar is 100 μm.

Table 1

	Antibodies and Concentrations		
	Antibody	**Vendor**	**Concentration**
Primary Antibodies	Mouse x Nestin	Millipore, Ref. # MAB353	1:100
	Mouse x Neuronal Nuclei (NeuN)	Millipore Ref. # MAB377	1:500
	Mouse x O1	Millipore, Ref. # MAB344	1:25
	Rabbit x Beta-3-Tubulin (B3T)	ABCAM, Ref. #ab18707	1:500
	Chicken x Olig2	AVES, Ref. #OLIG2-0020	1:500
	Rabbit x Collagen IV	ABCAM, Ref. #ab6586	1:150
	Rat x Heparan Sulfate (HSPG2)	ABCAM, Ref. #ab2501	1:500
	Rat x Myelin Basic Protein (MBP)	BioRad, Ref. #MCA409S	1:250
	Chicken x Glial fibrillary acidic protein (GFAP)	Millipore, Ref, #ab5541	1:200
	Rabbit x Iba-1	WAKO, Ref. #019-19741	1:500
	Mouse x B3T	ABCAM, Ref.#ab78078	1:500
	Rabbot x Laminin	Sigma, Ref. #L9393	1:25
	Chicken x MAP2	Synaptic Systems, Ref. #18806	1:250
	Rabbit x NG2	Sigma, Ref. #AB5320	1:250
	Lectin from Wisteria Floribunda (WFA)	Millipore, Ref. #L1516	1:500
Secondary Antibodies	goat anti-chk Alexa Fluor (AF) 488	Invitrogen, Ref. #A11039	1:800
	goat anti-rab AF 635	Invitrogen, Ref. #A31577	1:800
	goat anti-rat AF 647	Invitrogen, Ref. #A21247	1:800
	goat anti-chk AF 555	Invitrogen, Ref. #A21437	1:800
	goat anti-rab AF 555	Invitrogen, Ref. #A21428	1:800
	goat anti-mo Cy3	Jackson ImmunoResearch, Ref. #115-165-068	1:800
	Cy2-Streptavidin	Jackson ImmunoResearch, Ref. #016-220-084	1:800
	goat anti-rab AF 488	Invitrogen, Ref. #A21311	1:800
	DAPI	ThermoScientfic, Ref. #62248	1:1000

References

[1] (2023, April 5). *Alzheimer's Disease Fact Sheet*. NIH National Institute of Aging. https://www.nia.nih.gov/health/alzheimers-and-dementia/alzheimers-disease-fact-sheet#:~:text=Estimates%20vary%2C%20but%20experts%20suggest,of%20dementia%20among%20older%20adults

[2] (2023 Alzheimer's disease facts and figures. (2023). Alzheimers Dement, 19(4), 1598-1695. https://doi.org/10.1002/alz.13016

[3] Henstridge, C. M., Hyman, B. T., & Spires-Jones, T. L. (2019). Beyond the neuron-cellular interactions early in Alzheimer disease pathogenesis. Nat Rev Neurosci, 20(2), 94-108. https://doi.org/10.1038/s41583-018-0113-1

[4] Rathinam, C., Poueymirou, W. T., Rojas, J., Murphy, A. J., Valenzuela, D. M., Yancopoulos, G. D., Rongvaux, A., Eynon, E. E., Manz, M. G., & Flavell, R. A. (2011). Efficient differentiation and function of human macrophages in humanized CSF-1 mice. Blood, 118(11), 3119-3128. https://doi.org/10.1182/blood-2010-12-326926).

[5] Chen, G., Xu, T., Yan, Y., Zhou, Y., Jiang, Y., Melcher, K., & Xu, H. E. (2017). Amyloid beta: Structure, biology and structure-based therapeutic development. *Acta Pharmacologica Sinica*, *38*(9), 1205-1235. https://doi.org/10.1038/aps.2017.28

[6] Fattorelli, N., Martinez-Muriana, A., Wolfs, L., Geric, I., De Strooper, B., & Mancuso, R. (2021). Stem-cell-derived human microglia transplanted into mouse brain to study human disease. Nat Protoc, 16(2), 1013-1033. https://doi.org/10.1038/s41596-020-00447-4

[7] Wilson DM 3rd, Cookson MR, Van Den Bosch L, Zetterberg H, Holtzman DM, Dewachter I. Hallmarks of neurodegenerative diseases. Cell. 2023 Feb 16;186(4):693-714. doi: 10.1016/j.cell.2022.12.032.

[8] Sinha, S., & Lieberburg, I. (1999). Cellular mechanisms of beta-amyloid production and secretion. Proc Natl Acad Sci U S A, 96(20), 11049-11053. https://doi.org/10.1073/pnas.96.20.11049

[9] Oddo S, Caccamo A, Smith IF, Green KN, LaFerla FM. A dynamic relationship between intracellular and extracellular pools of Abeta. Am J Pathol. 2006 Jan;168(1):184-94. doi: 10.2353/ajpath.2006.050593.

[10] Roher AE, Lowenson JD, Clarke S, Woods AS, Cotter RJ, Gowing E, Ball MJ. beta-Amyloid-(1-42) is a major component of cerebrovascular amyloid deposits: implications for the pathology of Alzheimer disease. Proc Natl Acad Sci U S A. 1993 Nov 15;90(22):10836-40. doi: 10.1073/pnas.90.22.10836.

[11] Bloom GS. Amyloid-β and tau: the trigger and bullet in Alzheimer disease pathogenesis. JAMA Neurol. 2014 Apr;71(4):505-8. doi: 10.1001/jamaneurol.2013.5847. PMID: 24493463.

[12] Hampel, H., Hardy, J., Blennow, K., Chen, C., Perry, G., Kim, S. H., Villemagne, V. L., Aisen, P., Vendruscolo, M., Iwatsubo, T., Masters, C. L., Cho, M., Lannfelt, L., Cummings, J. L., & Vergallo, A. (2021). The Amyloid-β Pathway in Alzheimer's Disease. Molecular Psychiatry, 26(10), 5481-5503. https://doi.org/10.1038/s41380-021-01249-0

[13] Selkoe DJ. Alzheimer's disease: genes, proteins, and therapy. Physiol Rev. 2001;81:741–766

[14] Hansen DV, Hanson JE, Sheng M. Microglia in Alzheimer's disease. J Cell Biol. 2018 Feb 5;217(2):459-472. doi: 10.1083/jcb.201709069. Epub 2017 Dec 1.

[15] Heneka MT, Carson MJ, El Khoury J, Landreth GE, Brosseron F, Feinstein DL, Jacobs AH, Wyss-Coray T, Vitorica J, Ransohoff RM, Herrup K, Frautschy SA, Finsen B, Brown GC, Verkhratsky A, Yamanaka K, Koistinaho J, Latz E, Halle A, Petzold GC, Town T, Morgan D, Shinohara ML, Perry VH, Holmes C, Bazan NG, Brooks DJ, Hunot S, Joseph B, Deigendesch N, Garaschuk O, Boddeke E, Dinarello CA, Breitner JC, Cole GM, Golenbock DT, Kummer MP. Neuroinflammation in Alzheimer's disease. Lancet Neurol. 2015 Apr;14(4):388-405. doi: 10.1016/S1474-4422(15)70016-5.

[16] Abud, E. M., Ramirez, R. N., Martinez, E. S., Healy, L. M., Nguyen, C. H. H., Newman, S. A., Yeromin, A. V., Scarfone, V. M., Marsh, S. E., Fimbres, C., Caraway, C. A., Fote, G. M., Madany,

A. M., Agrawal, A., Kayed, R., Gylys, K. H., Cahalan, M. D., Cummings, B. J., Antel, J. P., . . . Blurton-Jones, M. (2017). iPSC-Derived Human Microglia-like Cells to Study Neurological Diseases. Neuron, 94(2), 278-293 e279. https://doi.org/10.1016/j.neuron.2017.03.042;

[17] Leng, F., & Edison, P. (2021). Neuroinflammation and microglial activation in Alzheimer disease: where do we go from here? Nat Rev Neurol, 17(3), 157-172. https://doi.org/10.1038/s41582-020-00435-y

[18] Selkoe DJ, Hardy J. The amyloid hypothesis of Alzheimer's disease at 25 years. EMBO Mol Med. 2016 Jun 1;8(6):595-608. doi: 10.15252/emmm.201606210.

[19] Kametani F, Hasegawa M. Reconsideration of Amyloid Hypothesis and Tau Hypothesis in Alzheimer's Disease. Front Neurosci. 2018 Jan 30;12:25. doi: 10.3389/fnins.2018.00025.

[20] Hardy JA, Higgins GA. Alzheimer's disease: the amyloid cascade hypothesis. Science. 1992 Apr 10;256(5054):184-5. doi: 10.1126/science.1566067.

[21] Zhou, J., Yu, W., Zhang, M. *et al.* Imbalance of Microglial TLR4/TREM2 in LPS-Treated APP/PS1 Transgenic Mice: A Potential Link Between Alzheimer's Disease and Systemic Inflammation. *Neurochem Res* **44**, 1138–1151 (2019). https://doi.org/10.1007/s11064-019-02748-x

[22] (2023, March 1). Alzheimer's Disease Genetics Fact Sheet. NIH National Institute of Aging. https://www.nia.nih.gov/health/genetics-and-family-history/alzheimers-disease-genetics-fact-sheet

[23] Jansen IE, Savage JE, Watanabe K, Bryois J, Williams DM, Steinberg S, et al. Genome-wide meta-analysis identifies new loci and functional pathways influencing Alzheimer's disease risk. Nat Genet. 2019;51:404–13.

[24] Pimenova AA, Raj T, Goate AM. Untangling genetic risk for Alzheimer's disease. Biol Psychiatry. 2018;83:300–10

[25] Victor, M. B., Leary, N., Luna, X., Meharena, H. S., Scannail, A. N., Bozzelli, P. L., Samaan, G., Murdock, M. H., von Maydell, D., Effenberger, A. H., Cerit, O., Wen, H. L., Liu, L., Welch, G.,

Bonner, M., & Tsai, L. H. (2022). Lipid accumulation induced by APOE4 impairs microglial surveillance of neuronal-network activity. Cell Stem Cell, 29(8), 1197-1212 e1198. https://doi.org/10.1016/j.stem.2022.07.005

[26] Cohen RM, Rezai-Zadeh K, Weitz TM, Rentsendorj A, Gate D, Spivak I, Bholat Y, Vasilevko V, Glabe CG, Breunig JJ, Rakic P, Davtyan H, Agadjanyan MG, Kepe V, Barrio JR, Bannykh S, Szekely CA, Pechnick RN, Town T. A transgenic Alzheimer rat with plaques, tau pathology, behavioral impairment, oligomeric aβ, and frank neuronal loss. J Neurosci. 2013 Apr 10;33(15):6245-56. doi: 10.1523/JNEUROSCI.3672-12.2013.

[27] Usui T, Sakurai M, Kawasaki H, Ohama T, Yamawaki H, Sato K. Establishment of a novel three-dimensional primary culture model for hippocampal neurogenesis. Physiol Rep. 2017 Jun;5(12):e13318. doi: 10.14814/phy2.13318.

[28] Dingle, Y. L., Liaudanskaya, V., Finnegan, L. T., Berlind, K. C., Mizzoni, C., Georgakoudi, I., Nieland, T. J. F., & Kaplan, D. L. (2020). Functional Characterization of Three-Dimensional Cortical Cultures for In Vitro Modeling of Brain Networks. iScience, 23(8), 101434. https://doi.org/10.1016/j.isci.2020.101434

[29] Pang, Y., Zheng, B., Kimberly, S. L., Cai, Z., Rhodes, P. G., & Lin, R. C. (2012). Neuron-oligodendrocyte myelination co-culture derived from embryonic rat spinal cord and cerebral cortex. Brain Behav, 2(1), 53-67. https://doi.org/10.1002/brb3.33

[30] Atherton, E., Brown, S., Papiez, E. *et al.* Lipopolysaccharide-induced neuroinflammation disrupts functional connectivity and community structure in primary cortical microtissues. *Sci Rep* 11, 22303 (2021). https://doi.org/10.1038/s41598-021-01616-5

[31] Luchena C, Zuazo-Ibarra J, Valero J, Matute C, Alberdi E, Capetillo-Zarate E. A Neuron, Microglia, and Astrocyte Triple Co-culture Model to Study Alzheimer's Disease. Front Aging Neurosci. 2022 Apr 14;14:844534. doi: 10.3389/fnagi.2022.844534.

[32] McQuade, A., Coburn, M., Tu, C.H. *et al.* Development and validation of a simplified method to generate human microglia from pluripotent stem cells. *Mol Neurodegeneration* 13, 67 (2018). https://doi.org/10.1186/s13024-018-0297-x

[33] Kim SJ, Li J, Mahairaki V. Stem cell-derived three-dimensional (organoid) models of Alzheimer's disease: a precision medicine approach. Neural Regen Res. 2021 Aug;16(8):1546-1547. doi: 10.4103/1673-5374.303019.

[34] Pandya, H., Shen, M., Ichikawa, D. *et al.* Differentiation of human and murine induced pluripotent stem cells to microglia-like cells. *Nat Neurosci* 20, 753–759 (2017). https://doi.org/10.1038/nn.4534

[35] Takuya Yagi, Daisuke Ito, Yohei Okada, Wado Akamatsu, Yoshihiro Nihei, Takahito Yoshizaki, Shinya Yamanaka, Hideyuki Okano, Norihiro Suzuki, Modeling familial Alzheimer's disease with induced pluripotent stem cells, *Human Molecular Genetics*, Volume 20, Issue 23, 1 December 2011, Pages 4530–4539, https://doi.org/10.1093/hmg/ddr394

[36] Choi SH, Kim YH, Hebisch M, Sliwinski C, Lee S, D'Avanzo C, Chen H, Hooli B, Asselin C, Muffat J, Klee JB, Zhang C, Wainger BJ, Peitz M, Kovacs DM, Woolf CJ, Wagner SL, Tanzi RE, Kim DY. A three-dimensional human neural cell culture model of Alzheimer's disease. Nature. 2014 Nov 13;515(7526):274-8. doi: 10.1038/nature13800. Epub 2014 Oct 12.

[37] Hopkins, A. M., DeSimone, E., Chwalek, K., & Kaplan, D. L. (2015). 3D in vitro modeling of the central nervous system. Prog Neurobiol, 125, 1-25. https://doi.org/10.1016/j.pneurobio.2014.11.003

[38] Zhuang, P., Sun, A. X., An, J., Chua, C. K., & Chew, S. Y. (2018). 3D neural tissue models: From spheroids to bioprinting. Biomaterials, 154, 113-133. https://doi.org/10.1016/j.biomaterials.2017.10.002

[39] Rubashkin, M. G., Ou, G. & Weaver, V. M. Deconstructing signaling in three dimensions. Biochemistry 53, 2078–2090 (2014)

[40] Schell JY, Wilks BT, Patel M, Franck C, Chalivendra V, Cao X, Shenoy VB, Morgan JR. Harnessing cellular-derived forces in self-assembled microtissues to control the synthesis and alignment of ECM. Biomaterials. 2016 Jan;77:120-9. doi: 10.1016/j.biomaterials.2015.10.080. Epub 2015 Nov 2.

[41] Ravi M, Paramesh V, Kaviya SR, Anuradha E, Solomon FD. 3D cell culture systems: advantages and applications. J Cell Physiol. 2015 Jan;230(1):16-26. doi: 10.1002/jcp.24683.

[42] Lovett ML, Nieland TJF, Dingle YL, Kaplan DL. Innovations in 3-Dimensional Tissue Models of Human Brain Physiology and Diseases. Adv Funct Mater. 2020 Oct 28;30(44):1909146. doi: 10.1002/adfm.201909146. Epub 2020 Mar 4.

[43] Karahuseyinoglu S, Sekerdag E, Aria MM, et al. Three-dimensional neuron–astrocyte construction on matrigel enhances establishment of functional voltage-gated sodium channels. *J. Neurochem.* 2021; 156: 848–866. https://doi.org/10.1111/jnc.15185

[44] Dingle YT, Boutin ME, Chirila AM, Livi LL, Labriola NR, Jakubek LM, Morgan JR, Darling EM, Kauer JA, Hoffman-Kim D. Three-Dimensional Neural Spheroid Culture: An In Vitro Model for Cortical Studies. Tissue Eng Part C Methods. 2015 Dec;21(12):1274-83. doi: 10.1089/ten.TEC.2015.0135. Epub 2015 Oct 6.

[45] Pampaloni, F., Reynaud, E. & Stelzer, E. The third dimension bridges the gap between cell culture and live tissue. *Nat Rev Mol Cell Biol* 8, 839–845 (2007). https://doi.org/10.1038/nrm2236

[46] Sun, M., Liu, A., Yang, X., Gong, J., Yu, M., Yao, X., Wang, H., & He, Y. (2021). 3D Cell Culture—Can It Be As Popular as 2D Cell Culture? *Advanced NanoBiomed Research*, *1*(5), 2000066. https://doi.org/10.1002/anbr.202000066

[47] Brown S, Atherton E, Borton DA. A Three-Dimensional Primary Cortical Culture System Compatible with Transgenic Disease Models, Virally Mediated Fluorescence, and Live Microscopy. Methods Mol Biol. 2023;2683:153-167. doi: 10.1007/978-1-0716-3287-1_12.

[48] Atherton, E., Hu, Y., Brown, S., Papiez, E., Ling, V., Colvin, V. L., & Borton, D. A. (2022). A 3D in vitro model of the device-tissue interface: functional and structural symptoms of innate

neuroinflammation are mitigated by antioxidant ceria nanoparticles. *Journal of Neural* Engineering, 19(3), 036004. https://doi.org/10.1088/1741-2552/ac6908

[49] Fennema, E., Rivron, N., Rouwkema, J., van Blitterswijk, C. & De Boer, J. Spheroid culture as a tool for creating 3D complex tissues. Trends Biotechnol. 31, 108–115 (2013).

[50] Severino, F. P. U. *et al.* The role of dimensionality in neuronal network dynamics. *Sci. Rep.* 6, 1–14 (2016).

[51] Lam, D. *et al.* Tissue-specific extracellular matrix accelerates the formation of neural networks and communities in a neuron-glia co-culture on a multi-electrode array. *Sci. Rep.* 9, 1–15 (2019).

[52] Elder GA, Gama Sosa MA, De Gasperi R. Transgenic mouse models of Alzheimer's disease. Mt Sinai J Med. 2010 Jan-Feb;77(1):69-81. doi: 10.1002/msj.20159.

[53] Lok K, Zhao H, Shen H, Wang Z, Gao X, Zhao W, Yin M. Characterization of the APP/PS1 mouse model of Alzheimer's disease in senescence accelerated background. Neurosci Lett. 2013 Dec 17;557 Pt B:84-9. doi: 10.1016/j.neulet.2013.10.051. Epub 2013 Oct 28. PMID: 24176881.

[54] Chishti, M., Yang, D., Janus, C., Phinney, A. L., Horne, P., Pearson, J., Strome, R., Zuker, N., Loukides, J., French, J., Turner, S., Lozza, G., Grilli, M., Kunicki, S., Morissette, C., Paquette, J., Gervais, F., Bergeron, C., Fraser, P. E., . . . Westaway, D. (2001). Early-onset Amyloid Deposition and Cognitive Deficits in Transgenic Mice Expressing a Double Mutant Form of Amyloid Precursor Protein 695. *Journal of Biological Chemistry*, *276*(24), 21562-21570. https://doi.org/10.1074/jbc.M100710200

[55] Zhou, J., Yu, W., Zhang, M. *et al.* Imbalance of Microglial TLR4/TREM2 in LPS-Treated APP/PS1 Transgenic Mice: A Potential Link Between Alzheimer's Disease and Systemic Inflammation. *Neurochem Res* **44**, 1138–1151 (2019). https://doi.org/10.1007/s11064-019-02748-x

[56] Games D, Adams D, Alessandrini R, Barbour R, Berthelette P, Blackwell C, Carr T, Clemens J, Donaldson T, Gillespie F (1995) Alzheimer-type neuropathology in transgenic mice

overexpressing V717f beta-amyloid precursor protein. Nature 373:523–527, doi:10.1038/373523a0, pmid:7845465

[57] Jankowsky JL, Slunt HH, Ratovitski T, Jenkins NA, Copeland NG, Borchelt DR (2001) Co-expression of multiple transgenes in mouse CNS: a comparison of strategies. *Biomol Eng* 17:157–165, doi:10.1016/S1389-0344(01)00067-3, pmid:11337275

[58] Mucke L, Masliah E, Yu GQ, Mallory M, Rockenstein EM, Tatsuno G, Hu K, Kholodenko D, Johnson-Wood K, McConlogue L (2000) High-level neuronal expression of Abeta 1–42 in wild-type human amyloid protein precursor transgenic mice: synaptotoxicity without plaque formation. *J Neurosci* 20:4050–4058, pmid:10818140.

[59] Oddo S, Caccamo A, Shepherd JD, Murphy MP, Golde TE, Kayed R, Metherate R, Mattson MP, Akbari Y, LaFerla FM (2003) Triple-transgenic model of Alzheimer's disease with plaques and tangles: intracellular Abeta and synaptic dysfunction. *Neuron* 39:409–421, doi:10.1016/S0896-6273(03)00434-3, pmid:12895417

[60] Yang S, Smit AF, Schwartz S, Chiaromonte F, Roskin KM, Haussler D, Miller W, Hardison RC (2004) Patterns of insertions and their covariation with substitutions in the rat, mouse, and human genomes. Genome Res 14:517–527, doi:10.1101/gr.1984404, pmid:15059992.

[61] Martinez A, Hériché J-K, Calvo M, Tischer C, Otxoa-de-Amezaga A, Pedragosa J, Bosch A, Planas AM, Petegnief V. 2023 Characterization of microglia behaviour in healthy and pathological conditions with image analysis tools. Open Biol. 13: 220200. https://doi.org/10.1098/rsob.220200

[62] Ferreira, T., Blackman, A., Oyrer, J. et al. Neuronal morphometry directly from bitmap images. Nat Methods 11, 982–984 (2014). https://doi.org/10.1038/nmeth.3125

[63] Sergent-Tanguy, S., Michel, D. C., Neveu, I., & Naveilhan, P. (2006). Long-lasting coexpression of nestin and glial fibrillary acidic protein in primary cultures of astroglial cells with a major participation of nestin(+)/GFAP(-) cells in cell proliferation. J Neurosci Res, 83(8), 1515-1524. https://doi.org/10.1002/jnr.20846

[64] Bernal A, Arranz L. Nestin-expressing progenitor cells: function, identity and therapeutic implications. Cell Mol Life Sci. 2018 Jun;75(12):2177-2195. doi: 10.1007/s00018-018-2794-z. Epub 2018 Mar 14.

[65] Wu KH, Madigan MC, Billson FA, Penfold PL. Differential expression of GFAP in early v late AMD: a quantitative analysis. Br J Ophthalmol. 2003 Sep;87(9):1159-66. doi: 10.1136/bjo.87.9.1159.

[66] Muñoz-Castro, C., Noori, A., Magdamo, C.G. et al. Cyclic multiplex fluorescent immunohistochemistry and machine learning reveal distinct states of astrocytes and microglia in normal aging and Alzheimer's disease. J Neuroinflammation 19, 30 (2022). https://doi.org/10.1186/s12974-022-02383-4

[67] Paolicelli, R. C., Sierra, A., Stevens, B., Tremblay, E., Aguzzi, A., Ajami, B., Amit, I., Audinat, E., Bechmann, I., Bennett, M., Bennett, F., Bessis, A., Biber, K., Bilbo, S., Blurton-Jones, M., Boddeke, E., Brites, D., Brône, B., Brown, G. C., . . . Wyss-Coray, T. (2022). Microglia states and nomenclature: A field at its crossroads. Neuron, 110(21), 3458. https://doi.org/10.1016/j.neuron.2022.10.020

[68] Kettenmann H, Hanisch UK, Noda M, Verkhratsky A. Physiology of microglia. Physiol Rev. 2011 Apr;91(2):461-553. doi: 10.1152/physrev.00011.2010.

[69] Marangon, D., Caporale, N., Boccazzi, M., Abbracchio, M. P., Testa, G., & Lecca, D. (2021). Novel in vitro Experimental Approaches to Study Myelination and Remyelination in the Central Nervous System. Front Cell Neurosci, 15, 748849. https://doi.org/10.3389/fncel.2021.748849

[70] Call, C. L., & Bergles, D. E. (2021). Cortical neurons exhibit diverse myelination patterns that scale between mouse brain regions and regenerate after demyelination. Nature Communications, 12(1), 1-15. https://doi.org/10.1038/s41467-021-25035-2

[71] Bechler, M. E., Byrne, L., & Ffrench-Constant, C. (2015). CNS Myelin Sheath Lengths Are an Intrinsic Property of Oligodendrocytes. Curr Biol, 25(18), 2411-2416. https://doi.org/10.1016/j.cub.2015.07.056

[72] Fernandez CG, Hamby ME, McReynolds ML, Ray WJ. The Role of APOE4 in Disrupting the Homeostatic Functions of Astrocytes and Microglia in Aging and Alzheimer's Disease. Front Aging Neurosci. 2019 Feb 11;11:14. doi: 10.3389/fnagi.2019.00014.

[73] Mayoral SR, Etxeberria A, Shen YA, Chan JR. Initiation of CNS Myelination in the Optic Nerve Is Dependent on Axon Caliber. Cell Rep. 2018 Oct 16;25(3):544-550.e3. doi: 10.1016/j.celrep.2018.09.052.